

## Towards a Fundamental Understanding of the Lithium Metal Anode in Solid State Batteries - An Electrochemo-Mechanical Study on the Garnet-type Solid Electrolyte $\text{LiAlLaZrO}$

Thorben Krauskopf, Hannah Hartmann, Wolfgang G. Zeier, and Jürgen Janek

ACS Appl. Mater. Interfaces, **Just Accepted Manuscript** • DOI: 10.1021/acsami.9b02537 • Publication Date (Web): 20 Mar 2019

Downloaded from <http://pubs.acs.org> on March 21, 2019

### Just Accepted

"Just Accepted" manuscripts have been peer-reviewed and accepted for publication. They are posted online prior to technical editing, formatting for publication and author proofing. The American Chemical Society provides "Just Accepted" as a service to the research community to expedite the dissemination of scientific material as soon as possible after acceptance. "Just Accepted" manuscripts appear in full in PDF format accompanied by an HTML abstract. "Just Accepted" manuscripts have been fully peer reviewed, but should not be considered the official version of record. They are citable by the Digital Object Identifier (DOI®). "Just Accepted" is an optional service offered to authors. Therefore, the "Just Accepted" Web site may not include all articles that will be published in the journal. After a manuscript is technically edited and formatted, it will be removed from the "Just Accepted" Web site and published as an ASAP article. Note that technical editing may introduce minor changes to the manuscript text and/or graphics which could affect content, and all legal disclaimers and ethical guidelines that apply to the journal pertain. ACS cannot be held responsible for errors or consequences arising from the use of information contained in these "Just Accepted" manuscripts.

# Towards a Fundamental Understanding of the Lithium Metal Anode in Solid State Batteries - An Electrochemo-Mechanical Study on the Garnet-type Solid Electrolyte $\text{Li}_{6.25}\text{Al}_{0.25}\text{La}_3\text{Zr}_2\text{O}_{12}$

*Thorben Krauskopf<sup>a</sup>, Hannah Hartmann<sup>a</sup>, Wolfgang G. Zeier<sup>a,b</sup> and Jürgen Janek<sup>a,b\*</sup>*

<sup>a</sup>Institute of Physical Chemistry, Justus-Liebig-University Giessen, Heinrich-Buff-Ring 17, D-35392 Giessen, Germany.

<sup>b</sup>Center for Materials Research (LaMa), Justus-Liebig-University Giessen, Heinrich-Buff-Ring 16, D-35392 Giessen, Germany.

## KEYWORDS

solid-state battery, solid electrolyte, lithium metal anode, LLZO, interface, vacancy diffusion, current constriction, pressure dependence

## ABSTRACT

For the development of next generation lithium batteries, major research effort is spent to enable a reversible lithium metal anode by the use of solid electrolytes. However, the fundamentals of the solid-solid interface and especially the processes that take place under current load are still not well characterized. By measuring pressure dependent electrode kinetics, we explore the electrochemo-mechanical behavior of the lithium metal anode on the garnet electrolyte  $\text{Li}_{6.25}\text{Al}_{0.25}\text{La}_3\text{Zr}_2\text{O}_{12}$ . Due to the stability against reduction in contact with lithium metal, this serves as an optimal model system for kinetic studies without electrolyte degradation. We show that the interfacial resistance becomes negligibly small and converges to practically zero  $\Omega \cdot \text{cm}^2$  at high pressure, i.e. at several hundred MPa external load. To the best of our knowledge, this is the smallest reported interfacial resistance in literature without the need for any interlayer. We interpret this observation by the concept of constriction resistance and show that the contact geometry in combination with the ionic transport in the solid electrolyte dominates the interfacial contributions for a clean interface in equilibrium. Furthermore, we show that – under anodic operating conditions – the vacancy diffusion limitation in the lithium metal restricts the rate capability of the lithium metal anode due to contact loss caused by vacancy accumulation

and the resulting pore formation near the interface. Results of a kinetic model show that the interface remains morphologically stable only when the anodic load does not exceed a critical value of approximately  $100 \mu\text{A}\cdot\text{cm}^{-2}$ , which is not high enough for practical cell setups employing a planar geometry. We highlight that future research on lithium metal anodes on solid electrolytes needs to focus on the transport within and the morphological instability of the metal electrode. Overall, the results help to develop a deeper understanding of the lithium metal anode on solid electrolytes and the major conclusions are not limited to the  $\text{Li}|\text{Li}_{6.25}\text{Al}_{0.25}\text{La}_3\text{Zr}_2\text{O}_{12}$  interface.

## INTRODUCTION

The application of the lithium metal anode in lithium ion batteries could offer cells with high energy density due to the very high theoretical capacity of lithium ( $3860 \text{ mAh}\cdot\text{g}^{-1}$  or  $2061 \text{ mAh}\cdot\text{cm}^{-3}$ ). Thus, great research effort has been put to replace the graphite anode by lithium metal, which would offer about a tenfold higher theoretical capacity on the anode side. However, no solution is yet found to prevent the problems of consumptive side reactions and dendrite formation in cells with liquid electrolytes.<sup>1–4</sup> When solid electrolytes with concurring ionic conductivity were developed, they were considered to be able to suppress lithium dendritic growth due to their high modulus and therefore enable the lithium metal anode.<sup>5</sup> Nevertheless, several problems still remain for the lithium metal|solid electrolyte interface. Solid electrolyte interphase (SEI) formation in contact with lithium is also observed in many solid electrolytes due to their narrow electrochemical window.<sup>6,7</sup>  $\text{Li}_7\text{La}_3\text{Zr}_2\text{O}_{12}$  (LLZO) is so far the only sufficiently “fast” solid electrolyte that shows adequate stability in contact with lithium metal.<sup>8</sup> For some time it was assumed that the interface resistance between LLZO and lithium metal is intrinsically high, until lithium carbonate was found to hinder the lithium ion transfer across the interface.<sup>10,11</sup> Sharafi et al. recently showed that indeed the  $\text{Li}|\text{LLZO}$  interface has only a negligible interfacial resistance when the surfaces are cleaned thoroughly.<sup>12</sup> Although a lot of work has been done to improve the interface kinetics using different interlayers and cleaning protocols,<sup>13–19</sup> the mechanistic understanding of the processes that take place at the interface during cycling is still elusive due to the absence of time resolved *operando* techniques and the buried nature of the interface.<sup>20</sup> However, the kinetics of the interface and its morphological stability will determine whether solid batteries with lithium metal anode can have a technological future.

In general, AC impedance spectroscopy is employed before and after lithium shuttling experiments on solid electrolytes to see dynamic changes of the interface. The increasing interfacial impedance during cycling was believed to be caused by the deterioration of the physical contact.<sup>21</sup> Koshikawa et al. were the first who were able to separate dynamic changes during dissolution and deposition at the Li|LLZO interface by introducing a reference electrode (RE).<sup>22</sup> It was suspected that void formation that exclusively takes place under anodic load might be the major reason for the sluggish performance. But unambiguous experimental evidence for the microstructural changes has not been provided yet.

Taking a deeper look into the mechanistic origin of this interface deterioration, vacancy injection at the interface is widely believed to be the kinetic limitation of the lithium metal anode during anodic dissolution.<sup>23</sup> In this context, it needs to be emphasized that the kinetics of parent metal anodes has long been subject of research. First and foremost, the Ag|AgX interface is one of the deepest investigated systems due to the chemical stability of the solid electrolytes.<sup>24</sup> In fact, Ag|AgX electrodes can be considered as a model case. During metal stripping it was observed that various processes take place at the metal|solid electrolytes interface that can lead to morphological instabilities. Every stripped metal atom injects a vacancy into the metal electrode, which will accumulate to pores if supersaturation due to high dissolution (anodic) currents occurs. These pores can exchange metal atoms and equilibrate their sizes, a process that has been called electrochemical Ostwald ripening.<sup>25</sup> This gradually leads to increasing contact loss between the parent electrode and the solid electrolyte. However, plastic deformation due to dislocation formation, movement and relaxation upon external pressure was found to maintain the interfacial contact, but very high pressures in the range of 300 MPa were required to achieve reasonable contact between Ag and Ag<sub>4</sub>RbI<sub>5</sub>.<sup>26</sup> Mechanical loads that are applied perpendicular to a solid|solid interface can in principle affect the kinetics in various ways and it has even been shown that periodic oscillations of the interfacial overpotentials of the Ag|AgI interface exist during anodic load in definite range of applied force.<sup>27–29</sup> All these mechanical considerations may also play a major role in the performance of lithium metal solid state batteries, but still have to be experimentally proven. While the mechanical aspects of the lithium metal itself recently gain more attention,<sup>30,31</sup> an up to date in-depth chemo-mechanical analysis of the Li|LLZO interface cannot be found in the literature yet.

In this work, we use Li<sub>6.25</sub>Al<sub>0.25</sub>La<sub>3</sub>Zr<sub>2</sub>O<sub>12</sub> as a model lithium solid electrolyte due to its intrinsic stability against lithium metal. SEI formation does not interfere with charge transfer kinetics – as in all other cases of unstable lithium solid electrolytes – and an in depth analysis of the

interface under dynamic conditions is feasible.<sup>7,32–34</sup> We prove the critical influence of mechanical forces on the interface kinetics of the lithium metal anode on LLZO and demonstrate that charge-transfer driven morphological instabilities and diffusion processes at the metal anode side strongly influence the overall cycling behavior. By performing pressure and temperature dependent measurements of the electrode kinetics, we corroborate that the intrinsic Li|LLZO interfacial resistance is indeed negligibly small if no contamination layer is present and that constriction resistances – often denoted as spreading resistances – in addition to contamination layers are responsible for the low exchange current densities reported in literature – like in the case of silver electrodes on solid electrolytes.<sup>12,35,36</sup> Constriction resistances are electrical contact resistances that are caused due to insufficient contact between electrical conductors and the resulting current line bundling near discrete contact spots.<sup>37</sup> By having a clean interface and negligible interface resistance, we introduce a new methodology to enable the separate analysis of the dissolution and deposition behavior of the metal anode without the need for an error prone reference electrode. The use of galvanostatic electrochemical impedance spectroscopy (GEIS) enables the separation of electrode impedances in two-electrode cells under operating conditions, which gives valuable insights into the electrode processes. We then show that, besides the lithium penetration during cathodic polarization,<sup>38</sup> pore formation due to vacancy accumulation under anodic load is indeed the major factor that will limit the development of solid lithium metal anode based batteries. In fact, the intrinsic morphological instability of parent metal electrodes on solid electrolytes impedes stable and reversible operation at low pressure normal to the interface. Depending on the applied mechanical pressure, mechanical phenomena have a very strong effect on the interface kinetics due to plastic deformation of lithium. On a microscopic level, the deformation is mainly affected by creep enabled by dislocation movement. We like to note that the intrinsic morphological instability of parent metal electrodes is a general phenomenon, which will be observed in any solid electrolyte system, independent of the specific chemistry. Differences in the occurrence of instabilities and their influence on the charge transfer kinetics will mainly depend on the mechanical properties of the metal and the solid electrolyte.

## EXPERIMENTAL SECTION

**Preparation of LLZO Solid Electrolyte.**  $\text{Li}_{6.25}\text{Al}_{0.25}\text{La}_3\text{Zr}_2\text{O}_{12}$  was prepared using a classical solid-state synthetic route.  $\text{Li}_2\text{CO}_3$  (> 99.0 %, Sigma-Aldrich),  $\text{La}(\text{OH})_3$  (99.9 %, Sigma-Aldrich),  $\text{Al}_2\text{O}_3$  (99.8 %, abcr) and  $\text{ZrO}_2$  nanopowder (< 100 nm, Sigma-Aldrich) were mixed

in stoichiometric ratio. No excess of lithium carbonate was used for the synthesis. 12 g of the mixture were ball milled (Fritsch Pulverisette 7 Premium Line) at 350 rpm using a ZrO<sub>2</sub> milling set (80 mL bowl and 120 g of balls with a diameter of 3 mm). The milling was performed 12 h with intermediate cooling times (every 10 min for 20 min). The resulting mixture was ground in a mortar and ball milled with the same milling parameters a second time. The homogenized powder was then pressed into pellets (6 g, 25 mm diameter) at a uniaxial force of 20 kN. Calcination was performed for 4 h at 1000 °C (100 °C·min<sup>-1</sup>) in open MgO crucibles inside a tube furnace (Nabertherm R40/500/13-P320) under 150 sccm dry oxygen. All following steps were performed under exclusion of humidity (H<sub>2</sub>O and CO<sub>2</sub>) to prevent Li<sup>+</sup>/H<sup>+</sup> exchange and carbonate formation.<sup>11,39,40</sup> Calcined pellets were ground to powder and ball milled in 5 g batches for 20 h at 350 rpm with intermediate cooling times (every 10 min for 20 min) using 90 g of ZrO<sub>2</sub> balls. 600 mg of the resulting powder was isostatically pressed into pellets (10 mm diameter) at 400 MPa for 1 h. Four of the resulting pellets were placed inside a small MgO crucible (12 mm inner diameter) as one batch, thoroughly covered with sacrificial powder that was not milled and sintered inside a tube furnace under 150 sccm dry oxygen, using a multi-step heating schedule. Therefore, the furnace was heated to 900 °C kept at 900 °C for 5 h, heated to 1100 °C, kept at this temperature for 5 h, heated to 1230 °C and kept at 1230 °C for 15 h. Heating was performed at a rate of 100 °C·h<sup>-1</sup>. The very high amount of sacrificial powder effectively avoided unwanted lithium loss. The obtained pellets had a diameter of around 8.3 mm and a density of 95 ± 1 %.

**Material Characterization.** Phase purity of the LLZO was tested using a PANalytical Empyrean powder diffractometer in Bragg-Brentano  $\theta$ - $\theta$  geometry with Cu K $\alpha$  radiation [ $\lambda_1 = 1.5405980$  Å;  $\lambda_2 = 1.5444260$  Å;  $I(\lambda_2)/I(\lambda_1) = 0.5$ ]. Measurements were carried out in the  $2\theta$  range between 10° and 120° with a step size of 0.026°. For this purpose, one representative LLZO pellet was manually ground to powder and placed on (911)-oriented silicon zero background holder. A Pawley fit<sup>41</sup> was carried out using the TOPAS-Academic V6 software package (Bruker).<sup>42</sup> The profile was described using Thompson-Cox-Hastings pseudo-Voigt functions.

Raman spectroscopy was used to further investigate the phase purity and detect possible surface contaminations. Raman spectra were collected using a Senterra Raman spectrometer (Bruker) with an excitation wavelength of 532 nm. Data collection was performed in a spectral range from 80 to 1555 cm<sup>-1</sup> using a 50x objective and a power of 2 mW. A pellet was placed on a

homemade plastic sample holder and was sealed airtight with a cover glass using silicon vacuum grease inside the glovebox to prevent carbonate formation during measurement.

The microstructure of the pellets as well as the morphology of the Li|LLZO interface were investigated using a Carl Zeiss Ultra field emission scanning electron microscope (SEM) instrument (Merlin). Cross sections of pellets and disassembled cells were fractured manually. The air sensitive samples were transferred from the glovebox to the vacuum chamber of the SEM with the Leica transfer module system (EM VCT50).

**Cell Assembly and Electrochemical Measurements.** Ionic conductivity and grain boundary contributions of the LLZO pellets were measured with blocking Au|LLZO|Au cells. 200 nm thick gold electrodes with a diameter of 6 mm were vapor deposited using a homemade setup. The cells were afterwards sealed in pouch bags, such that all measurements were performed under argon atmosphere.

Measurements of the interface kinetics were performed with Li|LLZO|Li cells. The measurement of such symmetric cells does not allow for distinguishing the impedance contributions from both interface sides. Usually the resulting interface resistance is just divided by two. This simplification is only true for identical interfaces in equilibrium. Especially for experiments under current load (non-equilibrium) this two-electrode setup does not allow to measure the interface kinetics upon lithium dissolution or deposition separately for both electrodes. To overcome this problem a reference electrode (RE) can be introduced.<sup>22,43</sup> However, due to the complicated fabrication and placement of the RE in a solid state system, the measurements are highly error-prone and can lead to strong distortion of the impedance spectra.<sup>36,43–46</sup> Here, we use a novel methodology to overcome this problem. We take advantage of the resistance-free Li|LLZO interfaces (see Results & Discussion), which can be prepared by high pressure contact formation that do not show impedance changes upon cycling. By intentionally applying a lithium metal working electrode (WE) with a low load bearing contact area (i.e. high interfacial resistance) on the interfacial resistance-free Li|LLZO half cells (used as combined CE and RE), the dynamic changes observed during the electrochemical measurements of the resulting full cells are only caused by the lithium working electrode (WE) similar to a micro electrode setup. A schematic of the experimental procedure is shown in Figure 1.

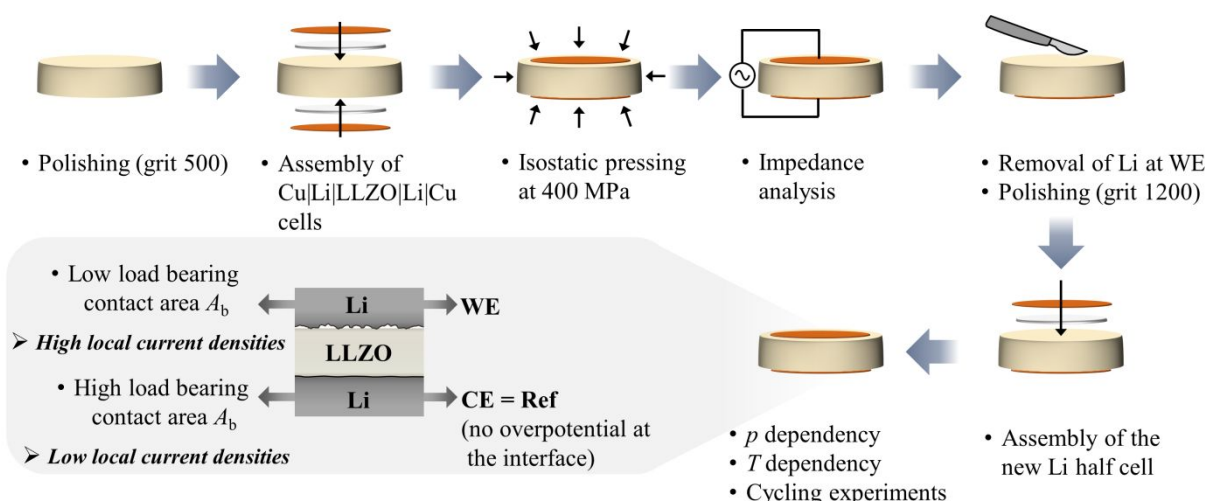


Figure 1: Experimental protocol for the manufacturing of interface resistance-free Li|LLZO half cells as CE for further analysis of the interfacial contributions of other WEs.

LLZO pellets were polished with sandpaper (500 grit SiC, Buehler, CarbiMet™) inside an argon-filled glovebox. Mechanically cleaned lithium foil disks (Rockwood Lithium GmbH, 120  $\mu\text{m}$  thickness) with a diameter of 6 mm were placed on both sides of the LLZO pellet and were covered with Cu thin foil disks with a diameter of 8 mm to ensure protection during pressing. These copper thin foil protected symmetric cells were vacuum sealed in three plastic envelopes (CPR GmbH, Sonodomen®) and pressed isostatically at 400 MPa resulting in a negligibly small interfacial resistance. This procedure was already shown to enable low-resistive contact between lithium and garnet materials.<sup>47–49</sup> Symmetric cells were tested with impedance analysis to ensure that the interfacial resistance contributions are indeed very small (below resolution of PEIS, i.e.  $< 1 \Omega \cdot \text{cm}^2$ ). Then one lithium electrode was removed with a scalpel and the open LLZO surface was mirror polished down to grit 1200. The resulting Li|LLZO half-cell was then combined with a new Li WE that was assembled in different ways, depending on the intended measurement.

To investigate the pressure dependence of the Li|LLZO interface in equilibrium, a homemade setup was used inside the glovebox. A schematic is shown in Figure S1a. The pressure perpendicular to the interface was adjusted via a screw. The torque was precisely adjusted by means of a spring balance. The resulting force on the interface was calibrated externally using the force sensor KMT55-20kN (Inelta Sensorsysteme GmbH & Co. KG). For cell assembly, lithium foil disks with a diameter of 6 mm were placed on both sides of a polished LLZO pellet and were covered with Cu thin foil disks to ensure protection during pressing and easy disassembly of the cells. The symmetric cells were contacted with two Ni-current collectors



and placed into the setup to perform the force dependent measurements in a range between 300 N and 2000 N (corresponding to  $\approx 10$  MPa – 40 MPa). Impedance spectra were recorded in the frequency range between 1 Hz to 1 MHz with an amplitude of 10 mV using a SP300 impedance analyzer (Bio-Logic). The area of the Li foil was determined after each measurement, because an increase of the geometrical (apparent) contact area was observed due to plastic deformation. Three equal measurements were evaluated together and the error bars in Figure 2b represent the standard deviation.

For pressure dependent cycling experiments, a different setup was used (see Figure S1b). In this setup the pressure was maintained using a metal spring without any pressure release over time. The pressure changes were recorded during measurement with an electronic force gauge (KMT55-20kN, Inelta Sensorsysteme GmbH & Co. KG). Experiments were performed in a climate chamber at 25 °C to prevent changes in the impedance due to temperature effects. The assembled Ni|Li|LLZO|Li|Ni cells (0.5 mm thick Ni disks) were sealed in pouch bags and placed into the inset of the cell setup.

For all Li cycling experiments, galvanostatic electrochemical impedance spectroscopy (GEIS) was applied. This rarely used method allows to record the impedance changes *operando* under galvanostatic load, which allows time resolved separation of the impedance contributions that cause the overpotential observed in the voltage profile. All experiments were performed at an apparent (geometrical) current density of  $100 \mu\text{Acm}^{-2}$  with a sinusoidal current amplitude of about  $10 \mu\text{Acm}^{-2}$  in the frequency range from 7 MHz to 1 Hz using a VMP300 impedance analyzer (Bio-Logic). One measurement lasts less than 30 s. This prevents a high distortion of the low frequency part of the impedance spectra due to the microstructural changes of the interface.

Temperature dependent electrochemical impedance spectroscopy measurements were conducted in the temperature range from 233 K to 333 K (climate chamber, Weiss Klimatechnik, 1 h equilibration time) using a Biologic SP300 impedance analyzer in the range of 7 MHz to 100 mHz with an amplitude of 10 mV.

Impedance spectra were fitted using the RelaxIS software package (rhd instruments, Version 3). At higher temperatures the grain boundary contribution became very small, preventing a reasonable fit. To still enable a correct data evaluation, the alpha value  $\alpha$  for the constant phase

element  $Q$  corresponding to the grain boundary process was fixed to a value estimated at lower temperatures and kept constant for GEIS measurements.

## RESULTS AND DISCUSSION

**Structural and Microstructural Characterization.** The combination of XRD and Raman spectroscopy reveal phase pure  $\text{Li}_{6.25}\text{Al}_{0.25}\text{La}_3\text{Zr}_2\text{O}_{12}$  specimen without  $\text{Li}_2\text{CO}_3$  contamination layers on the surface (See Figure S2). The SEM images in Figure S3 show mainly closed porosity in good accordance to the geometrical estimated relative density of  $95 \pm 1 \%$ . Details of the structural and microstructural characterization of the LLZO specimen are included in the SI.

**Pressure Dependence of the Interface Resistance in Equilibrium.** First, we discuss the pressure dependence of the Li|LLZO interface under equilibrium conditions, i.e. without current load that was measured on symmetric Li|LLZO|Li cells using potentiostatic electrochemical impedance spectroscopy (PEIS). Figure 2a shows pressure dependent Nyquist plots of the impedance spectra under different externally applied forces. The measurements were normalized to the Li disk diameter that was measured after each pressure dependent measurement and the interface resistance  $R_{\text{int}}$  was divided by a factor of two, because two interfaces were measured in this setup (See Figure S1a). It is obvious that the interface resistance  $R_{\text{int}}$  decreases strongly with external load.

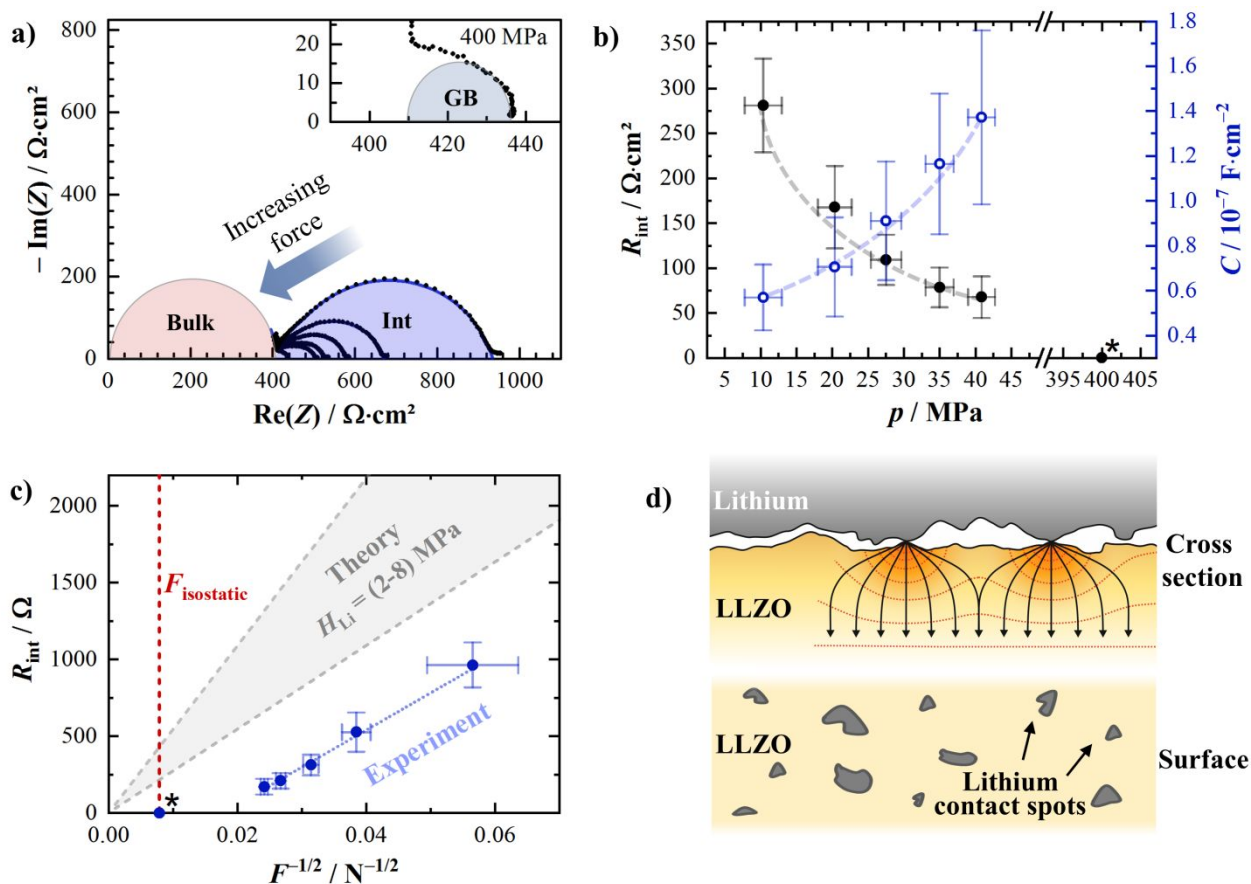


Figure 2: Pressure dependent Nyquist plots of Li|LLZO|Li cells showing the large impact of external force on the interface resistance  $R_{\text{int}}$  (a). (b) shows the measured interfacial resistances  $R_{\text{int}}$  as well as interface capacity values  $C$  as a function of the external pressure  $p$ . The obtained resistance values plotted vs  $F^{-1/2}$  show a linear relationship which is in agreement with theory of constriction resistances for electric contacts (c). Calculating the interface resistances assuming a Vickers Hardness for lithium in the range from 2-8 MPa gives the grey background area. The force corresponding to the isostatic pressure used in this work is marked as a vertical red dotted line. The measured interfacial resistance at this force (marked with a star) becomes negligible (d) Schematic representation of the Li|LLZO interface showing a few contact points as origin of constriction and the resulting bending of the current lines at the interface, which is the basis of the applied theory. At higher external forces, the contact spots increase their area due to the plastic deformation of the softer material (i.e. lithium). The arrows schematically indicate current lines. Equipotential lines are shown as red dotted lines.

Figure 2b shows the extracted interface resistance  $R_{\text{int}}$  vs the applied pressure. A clear decrease from around 300  $\Omega \cdot \text{cm}^2$  to around 50  $\Omega \cdot \text{cm}^2$  is observed in the investigated pressure range while the capacity of the interface increases by nearly a factor of three. The measured interface capacity values  $C$  are a function of the effective contact as well as the gap capacitance at the

interface. The physical origin of the interface capacity is discussed in more detail later on. It has to be noted that no large change of  $R_{\text{int}}$  was observed by maintaining the load for several minutes and that no increase of  $R_{\text{int}}$  was observed after releasing the pressure. This indicates that a permanent contact is formed that is mainly dependent on the maximum applied force during interface formation.

To understand the observed pressure-dependent interfacial resistance, the load bearing contact area  $A_b$  has to be introduced, which is the area of the effective contact between the electrode and the solid electrolyte. In practice  $A_b$  is much lower than the apparent contact area of the interface that is usually used to normalize the interfacial resistance in literature and also used here for the normalization of  $R_{\text{int}}$ , as the value of  $A_b$  is not accessible and thus unknown. However, the pressure-dependent measurement shows that the load bearing contact area  $A_b$  is highly dependent on the preparation route of the interface and especially the applied stack pressure. This behavior can be qualitatively understood using the theory of electrical constriction resistances<sup>37</sup> and was first mentioned for the Li|SE interface by Meyer et al.<sup>50</sup> This simple theory originally describes the contact resistance of monometallic contact surfaces by separate contact spots (or “ $a$ -spots”) that increase their contact area due to plastic deformation under an applied force. The distribution of these spots is defined by the small-scale surface roughness as schematically shown in Figure 2d. What follows is a  $1/F^{-1/2}$  relationship according to Equation 1, that is only dependent on the applied force  $F$  and the mechanical and electrical properties of the contacted materials. We apply this theory to the Li|LLZO interface and assume that the interface resistance does only depend on the constriction effect. Then the electric properties of LLZO and the plastic properties of lithium alone will determine the interfacial resistance, as the ionic conductivity of LLZO is much lower than the electronic conductivity of the lithium metal and the Vickers hardness of lithium with  $H_{\text{Li}} \leq 5 \text{ MPa}$ <sup>51</sup> is much lower than that of LLZO. Thus the plastic deformation of the lithium metal alone will dominate the changing contact area with external load. This implies that no contamination layer adds resistance to the Li|LLZO contacts, i.e. we assume in particular that a carbonate layer is not present (as shown above). If a resistive layer needs to be included, a correction term is added, that takes into account the blocking behavior of the impurity layer and explains the high interfacial resistances shown in literature.<sup>37</sup>

$$R_{\text{int}} = \frac{\rho}{2} \cdot \sqrt{\frac{\pi \cdot H}{F}} = \frac{1}{2 \cdot \sigma_{\text{Li}^+}} \cdot \sqrt{\frac{\pi \cdot H_{\text{Li}}}{F}} \quad (1)$$

In Equation 1,  $\sigma_{\text{Li}^+}$  denotes the ionic conductivity of LLZO that is  $0.46 \text{ mScm}^{-1}$  for our samples (see Table S1). The reported data for the elastic properties of lithium metal show a wide spread,<sup>30,52–56</sup> and therefore we use a range from 2 MPa to 8 MPa for the Vickers hardness. Figure 2c shows the theoretically estimated as well as the experimentally determined interfacial resistances. The experimental data show indeed the predicted  $F^{-1/2}$  relationship but an offset along the force axis is visible. While Equation 1 predicts that the interface resistance will become zero only at infinitely high force  $F$ , our experimental results imply that the interface resistance becomes zero already at a finite force. Various reasons might be responsible for this discrepancy. Equation 1 only holds for circular point contacts on ideally flat surfaces and is based on plastic deformation solely. Despite the polishing, there is still a high roughness on the micro scale (see Figure S4) which will result in non-uniform  $a$ -spots distributions and geometries. We want to highlight that this concept is based on the low scale roughness of the contact. Even microscopic cross section images can erroneously suggest well contact that is, however, not achieved on the atomic scale. Furthermore recent work on the elastic properties of bulk lithium metal shows the big role of creep on the deformation behavior under stress and suggests strain rate dependency.<sup>30,31</sup> Creep can enable deformation below the yield strength and might be the reason for the offset observed between experimental and theoretical data in Figure 2c. It has to be noted that the “history” of the lithium foil will also highly affect the texture and dislocation density of the lithium metal and thus the creep behavior which can also alter the pressure dependency.<sup>3</sup> Above all, equation 1 is not applicable at very high forces because of two reasons. Firstly equation 1 was established for  $a$ -spots of small size compared to their separating distance. When the nominal contact area  $A_c = F/H$  approaches the apparent one this simplification no longer applies.<sup>57</sup> Secondly for high ratios  $F/H$ ,  $A_c$  can become even larger than the apparent contact area. Thus a continuum-scale elastic-viscoplastic model needs to be applied on the interface geometry for further theoretical valuation as already reported by Narayan and Anand for simple asperity geometries.<sup>58</sup> The maintained good contact after pressure release might be the result of asperity flattening or asperity adhesion following to contact formation. The role of adhesion in relation to the interfacial kinetics was already reported by Wang and Sakamoto.<sup>53</sup>

By increasing the pressure to 400 MPa in an isostatic press setup – corresponding to a force of 16 kN – and relaxation to standard pressure, no interface resistance contributions were observed anymore, proving that the interface is not intrinsically highly resistive and that very high pressures are necessary at room temperature to obtain intimate and complete contact similarly

to observations for silver electrodes.<sup>26</sup> However, under this high load, plastic flow into the pores at the surface cannot be fully neglected<sup>58</sup> and the contact surface could be larger than the apparent one – depending on the surface roughness. The remaining second impedance contribution, beside the bulk process in the impedance spectra at 400 MPa (inset in Figure 2a) can clearly be assigned to grain boundaries in LLZO on the basis of temperature dependent measurements. An in-depth analysis of the different processes including bulk and grain boundary contributions follows in the next section.

To further validate the hypothesis that the kinetics of charge transfer at the Li|LLZO interface can be well described by the constriction resistance theory, we performed measurements at different temperature. The activation barrier for the charge transfer process is an intrinsic parameter and does not depend on the unknown contact area itself (but may depend on the distribution of difference surface sites). Its value should give valuable information about the nature of the interface.

**Temperature Dependence of the Interface Resistance.** If constriction resistances play the major role for the Li|LLZO interface kinetics, the activation barrier should be close to the activation energy of ion transport of LLZO inside the constriction zone.<sup>59</sup> Figure S5 shows impedance measurements of Au|LLZO|Au and Li|LLZO|Li cells in the temperature range between  $-10\text{ }^{\circ}\text{C}$  and  $-40\text{ }^{\circ}\text{C}$ . Different cell setups were necessary to enable the unequivocal assignment of the impedance responses to their underlying processes. For measurements with gold electrodes (Figure S5a), three processes can be distinguished: One parallel constant phase element (CPE)/resistor, a second constant phase element (CPE)/resistor as well as a CPE, representing the blocking electrodes. The first process with a characteristic apex frequency of  $f = 1.7 \cdot 10^5\text{ Hz}$  and a second one with an apex frequency of  $f = 1\text{ kHz}$  at  $-40\text{ }^{\circ}\text{C}$  can be assigned to bulk and grain boundary contributions respectively.<sup>60</sup> For a Li|LLZO|Li<sub>bc</sub> cell shown in Figure S5c, one side was intentionally assembled at low external force to enable a high interfacial resistance and thus a low load bearing contact area. For this cell setup, an additional contribution is visible, that is assigned to the Li|LLZO interface with a characteristic apex frequency of 90 Hz. It has to be noted, that the occurrence of two different relaxation times for the bulk and Li|LLZO interfacial process observed in the impedance spectra does not contradict that current constriction in the solid electrolyte mainly contributes to the interfacial impedance as shown by Fleig and Maier.<sup>59,61–63</sup> By preparing both interfaces at high pressure (see Figure S5e), the interfacial contribution vanishes and there are no hints for a Li|LLZO interfacial process, not even at  $-40\text{ }^{\circ}\text{C}$ . Therefore, the interface resistance must be in the range of  $0 \pm$

2  $\Omega \cdot \text{cm}^2$  at room temperature taking into account the resolution limit of the impedance measurement. Comparable low interfacial resistance values were already reported by Sharafi et al. for the bare Li|LLZO interface after performing a precondition step at 175 °C.<sup>12</sup>

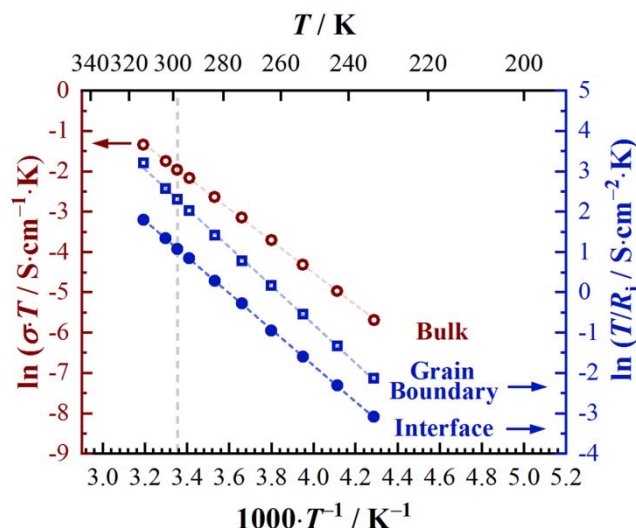


Figure 3: Arrhenius plot for a Li|LLZO|Li<sub>bc</sub> cell (e). Li<sub>bc</sub> denotes a lithium foil that was intentionally contacted with a low load bearing contact. Grain boundary charge transfer (blue open), bulk transport (red) and interface charge transfer (blue filled) can be clearly separated. The vertical dotted line represents room temperature.

All Arrhenius plots for the different cell setups provide in good agreement the same activation barriers for the distinctive processes bulk transport, grain boundary charge transfer and interface (see Figure S5b,d,f and exemplary Figure 3). To prevent wrong interpretation of the interfacial contribution of the Li|LLZO|Li<sub>bc</sub> cell due to temperature dependent contact geometry changes, multiple heating and cooling cycles were performed until no hysteresis was observed anymore. This is important to address the intrinsic property of the interface solely. The capacitances of the different processes were estimated at -40 °C using the Brug formula<sup>64</sup>, where  $\alpha$  denotes the ideality factor of the constant phase element (CPE) of the parallel combination R/CPE.

$$C = \left[ \frac{Q}{R^{1-\alpha}} \right]^{1/\alpha} \quad (2)$$

All extracted transport parameters can be found in Table S2. The capacitance values correspond well with the respective processes: bulk, grain boundary and interface.<sup>60</sup> However, the interface capacitance depends strongly on the gap capacitance<sup>59</sup> and is thus dependent on the contact

geometry itself. Table S1 summarizes the mean values that are important for the following discussion.

The grain boundary activation energy was found to be 30 % higher than for the bulk process in good accordance with theoretical predictions and reference data from experimental studies.<sup>53,65</sup> With the rough approximation that the grains are well fused together having an average diameter of 10  $\mu\text{m}$ , one grain boundary perpendicular to the current direction would have a resistivity of approximately  $(10 \cdot 10^{-3} \text{ mm} / 2 \text{ mm} \cdot 40 \Omega \cdot \text{cm}^2 = 0.2 \Omega \cdot \text{cm}^2)$  at room temperature. The grain boundary conductivity was estimated using a brick layer model and is around two orders of magnitude lower than the grain conductivity which was also predicted theoretically.<sup>65</sup> Details can be found in the SI.

**Discussion: Physico-Chemical Nature of the Interface in Equilibrium.** Figure 4 schematically summarizes the experimental findings for the different processes at the interface and inside the solid electrolyte. The following conclusions can be drawn:

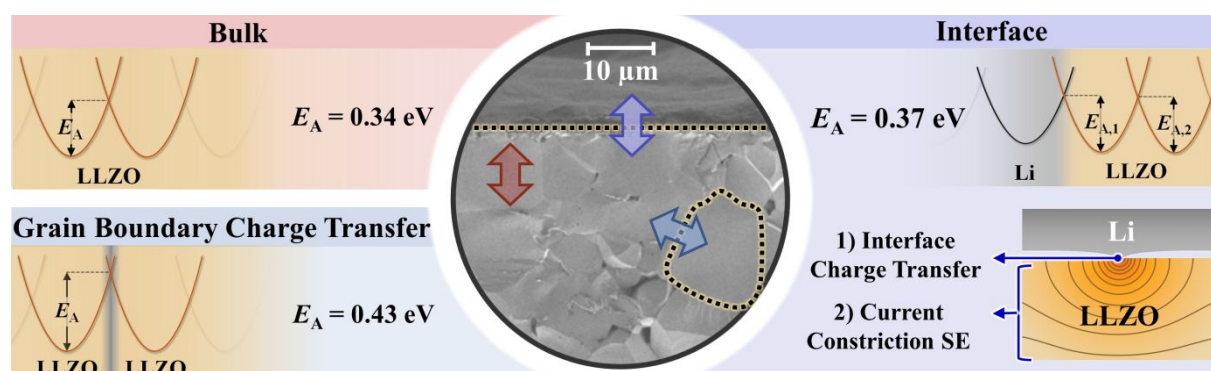


Figure 4: Schematic summarizing the activation energies measured with temperature dependent impedance spectroscopy. The interface contribution can be divided into the interface charge transfer and current constriction phenomena in the solid electrolyte near the interface, both being affected by the contact geometry as shown in the sketch on the bottom right.

- 1) The interface activation energy is close to the activation energy for lithium ion migration in the bulk electrolyte. Similar observations were also found for different Ta-substituted garnets.<sup>36</sup> This indicates that ion migration in the garnet phase rather than charge transfer  $\text{Li} = \text{Li}^+ + \text{e}'$  is the rate-limiting kinetic step.<sup>66</sup> We believe that the charge transfer impedance is so small, that it cannot be detected with impedance spectroscopy. Therefore we suggest that the interface kinetics are limited by current constriction in the solid electrolyte near the interface and thus the interfacial resistance can be better interpreted as spreading resistance, i.e. “contact geometry resistance”. Ion-transport limitation of the



Li|SE interface was also found by Lushta et al. on nanoscale experiments.<sup>67</sup> The slightly higher activation barrier of the interface in comparison to the bulk process observed in this study might be a result of the small deterioration of the first LLZO surface layer in contact with lithium metal due to a transition into the tetragonal phase as observed by Sakamoto and coworkers using TEM.<sup>68</sup> We like to note that the interface activation energy gets even closer to the bulk activation energy for higher interface resistances, i.e. for a smaller number of contact points and thus an expanded constriction zone, which supports the constriction concept (see Table S2).

- 2) The activation barrier for the interface is lower than for the grain boundaries, showing that the activation barrier to jump from grain to grain is higher than for the jump from the grain into active sites in the lithium metal or *vice versa*. Therefore, the area specific resistance should be lower than for the grain boundary process, i.e.  $0.2 \Omega \cdot \text{cm}^2$ , assuming a similar pre-factor.
- 3) If intimate contact between the solid electrolyte and lithium metal is achieved by high external loads and the absence of contamination layers, the interface resistance can become negligibly small.

These findings suggest that the interfacial charge transfer process itself is energetically only minimally more demanding than the bulk hopping process and will not hinder the development of solid state batteries with lithium metal anode. As one may assume a very small Debye length, we neglect space-charge layer effects for the sake of simplicity.<sup>69</sup> Unfortunately the load bearing contact area of the Li|SE interface is experimentally not accessible and no intrinsic value for the electrode resistance can be obtained. The microkinetic charge transfer resistance itself will also depend on the area density of active sites i.e. half crystal positions in the metal and the solid electrolyte which makes the analysis even more complex.<sup>66</sup>

**Non-Equilibrium - The Li|LLZO Interface under Current Load.** To investigate the kinetics of the interface separately during stripping and plating, a reference electrode is required.<sup>22</sup> Yet *operando* electrochemical measurements of the impedance during dc polarization are missing. GEIS measurements allow measuring the impedance response of a cell under current load. With this technique we can deconvolute the evolution of the different processes under working conditions.

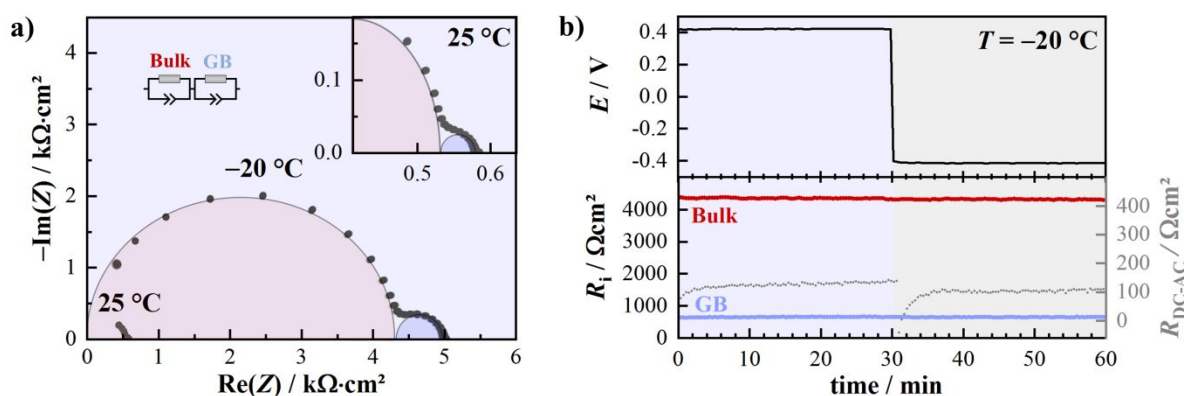


Figure 5: Results of a lithium stripping-plating GEIS experiment of a Li|LLZO|Li cell with electrodes prepared at high pressure ( $p = 400$  MPa) with negligible interface resistance at an apparent current density of  $100 \mu\text{A}\cdot\text{cm}^{-2}$ . a) Time resolved Nyquist plots of the cycling process at  $-20$  °C and  $25$  °C b) Voltage profile of stripping-plating experiments at  $-20$  °C. The fitted impedance contributions obtained from the analysis of the impedance spectra are on the bottom in (b). The discrepancy between the AC and DC signal is additionally shown as  $R_{\text{DC-AC}}$  in (b). The Nyquist plots do not show time dependent changes during an overall transported charge of  $50 \mu\text{Ah}\cdot\text{cm}^{-2}$ .

Figure 5a shows the Nyquist plots of the impedance spectra that were recorded *operando* during plating-stripping at  $100 \mu\text{A}\cdot\text{cm}^{-2}$  for ideally contacted Li|LLZO interfaces at  $25$  °C and  $-20$  °C. The impedance response includes only bulk and grain boundary contributions, and these are constant with time – even at  $-20$  °C. Figure 5b shows exemplary the potential profiles at  $-20$  °C. While the overpotential fits perfectly the impedance for  $t = 0$ , it slightly increases over time and reaches a steady state. These changes are not visible in the *operando* recorded impedance spectra in the frequency range up to  $1$  Hz. The additional area specific resistance, that is necessary to account for the entire voltage drop in the DC voltage profile was calculated according to Ohm's law and is denoted as  $R_{\text{DC-AC}}$ . The discrepancy between the estimated DC and AC resistances is only  $2.7\%$  at  $-20$  °C, but increases in percentage with rising temperature. Figure S6 shows further voltage profiles at different temperatures as well as the impedance deconvolution for  $T = 25$  °C. Further information about the temperature dependency can be found in the Supporting Information (Figure S7). The origin of  $R_{\text{DC-AC}}$  is yet unclear; it also appears in the impedance spectra in the frequency range below  $1$  Hz at high temperatures as a low frequency tail and we attribute it to diffusive processes, which we cannot identify using the current experimental data. Zhu et al. relate it to a few atomic layers thick “oxygen-deficient interphase” that forms at the interface.<sup>8</sup> However, the impedance spectra unambiguously prove that the interface itself does not age during stripping-plating at  $100 \mu\text{A}\cdot\text{cm}^{-2}$ .

In the following we exploit the kinetics of the (practically) ideally reversible electrodes of our Li|LLZO|Li cells, that have been prepared under strong applied pressure. As no impedance changes are observed at  $100 \mu\text{A}\cdot\text{cm}^{-2}$ , we can use half cells of this electrode type as counter and reference electrode at the same time, equivalent to a micro electrode setup with large counter electrode and are able to avoid an error-prone reference electrode.<sup>36,43–46</sup> By attaching the lithium metal WE at much lower pressure, we achieve a much lower load bearing contact area. The changes in the impedance are then only caused by the WE because the local current density is much higher than at the virtually ideal CE (see Figure 1). The local current density will be used as a terminus describing the current density of the active interface (corresponding to  $A_b$ ) as it is a better descriptor than the apparent geometrical current density. However, its value is not known and only relative changes can be evaluated. In comparison to measurements with a reference electrode, the introduced methodology additionally allows to detect changes in the bulk resistivity and is in principle able to give further insights into lithium penetrating behavior.

Figure 6 shows the measurement of a Li|LLZO|Li<sub>bc</sub> cell, where Li<sub>bc</sub> denotes the working electrode side that was prepared with only 35 MPa external pressure. Cycling was performed without any pressure at an apparent current density of  $100 \mu\text{A}\cdot\text{cm}^{-2}$ , thus, the local current density on the WE side is much higher. The Nyquist plots show three processes, which we interpret as bulk, grain boundary and interface contributions. During the dissolution process (see Figure 6a) the interface resistance at the WE side increases while the other contributions remain constant. The sequence of all recorded impedance spectra is shown in a phase angle vs frequency plot, to better see the temporal evolution. During deposition (Figure 6b), the interface resistance decreases again.

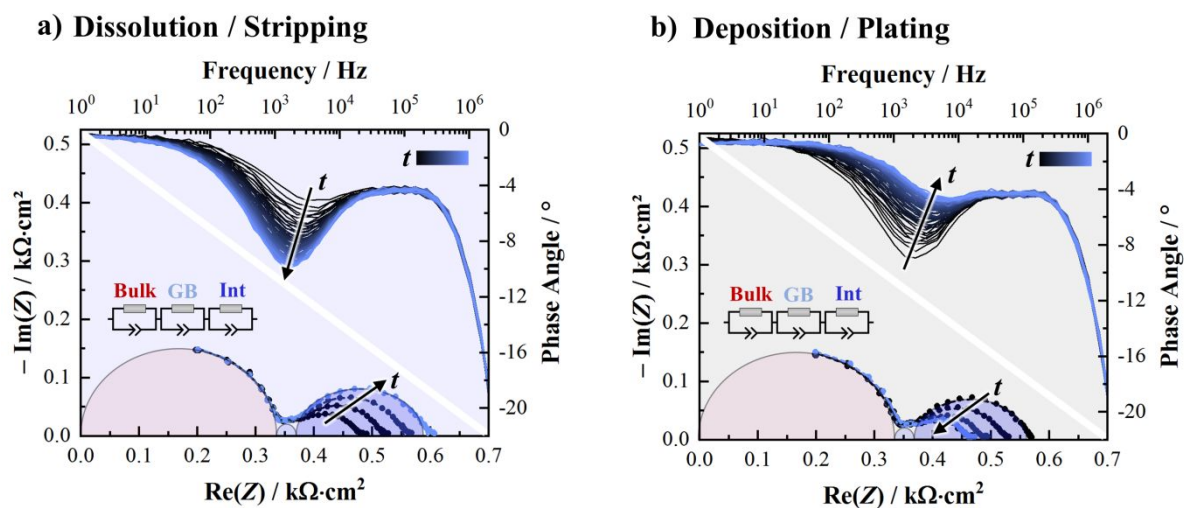


Figure 6: Results from a lithium stripping-plating GEIS measurements of a  $\text{Li}|\text{LLZO}|\text{Li}_{bc}$  cell with an apparent current density of  $100 \mu\text{A}\cdot\text{cm}^{-2}$ . Evolution of the impedance with time is shown in Nyquist representation as well as for all cycles in a phase angle vs frequency plot during the dissolution process (a) and the deposition process (b). Per cycle about 240 nm lithium was shuttled corresponding to area specific capacity of  $0.18 \text{ C}\cdot\text{cm}^{-2}$ .

To get deeper insights into the reasons for the evolution of the overvoltage, the fitted impedance contributions as well as the galvanostatic potential profile ( $100 \mu\text{A}\cdot\text{cm}^{-2}$ ) are shown in Figure 7a.

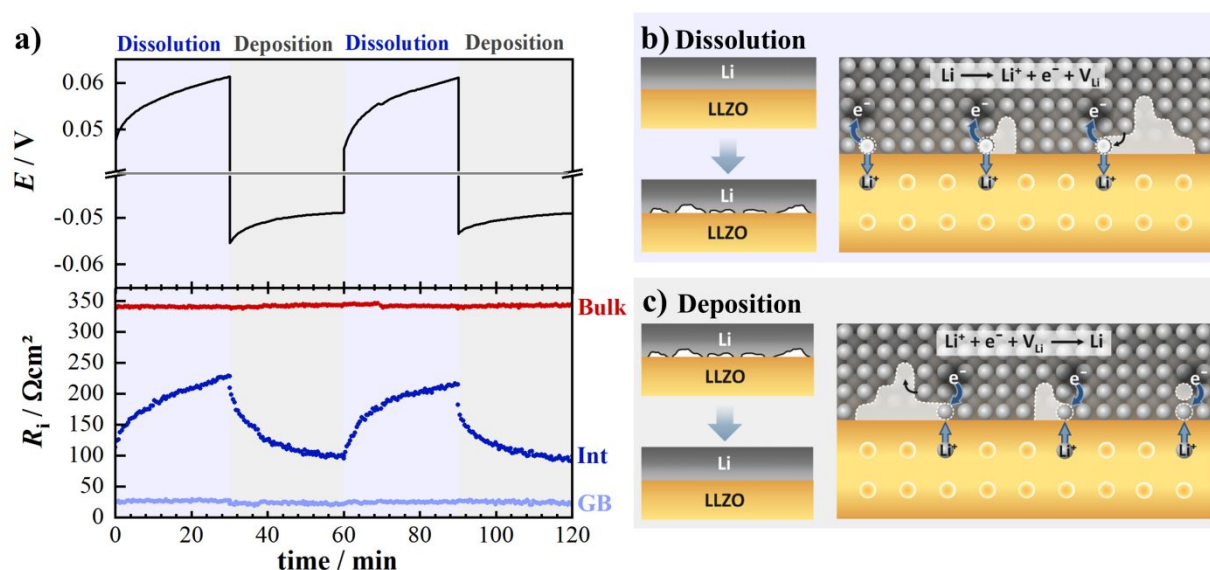


Figure 7: a) Voltage profile during dissolution and deposition experiments on a  $\text{Li}|\text{LLZO}|\text{Li}_{bc}$  cell at  $100 \mu\text{A}\cdot\text{cm}^{-2}$  and the corresponding fitted impedance contributions obtained from the impedance spectra in Figure 6. The dissolution process leads to contact loss observable in growing interfacial resistances whereas the deposition process seems to reversibly fill these pores attaining the initial contact again. The assumed processes are schematically shown on the right side for the dissolution process (b) and the deposition process (c) on the macroscopic and atomic scale.

Similar to the symmetrical cells with ideally reversible electrodes, no changes in the bulk and grain boundary process are observed, showing that no lithium infiltration takes place. The main reason for the increasing overpotential is thus mainly attributed to changes in the interfacial resistance.  $R_{\text{int}}$  increases during dissolution from around  $110 \Omega\cdot\text{cm}^2$  to  $230 \Omega\cdot\text{cm}^2$ . This behavior can be attributed to a reduction of the effective contact area (load bearing contact area  $A_b$ ) between the solid electrolyte and the lithium metal. After subsequent deposition, the

interface resistance nearly reaches its initial value showing a partial reversibility of the interface deterioration during short time cycling. Koshikawa et al. made similar observations using a reference electrode.<sup>22</sup>

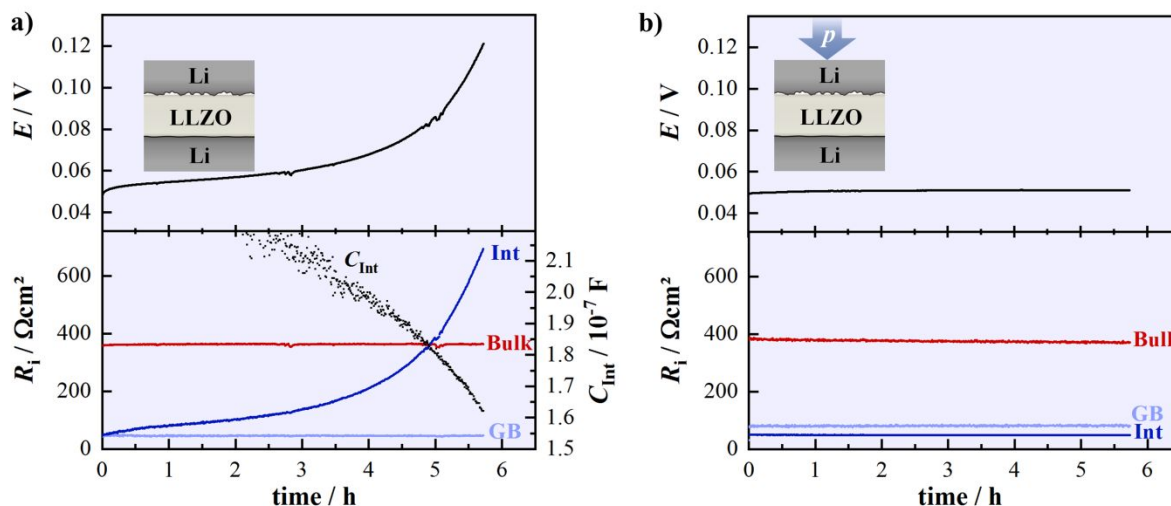


Figure 8: Results of long time lithium stripping experiments at  $100 \mu\text{A}\cdot\text{cm}^{-2}$  without externally applied pressure (a) and  $\approx 35 \text{ MPa}$  external applied pressure perpendicular to the interface (b). The voltage profile is shown as well as the area specific resistances that together cause the overpotential. By applying external pressure, pore formation that leads to contact loss is fully prevented.

Contact loss due to pore formation at the interface is probably the reason for the change of the interface resistance as shown schematically in Figure 7b. To corroborate this hypothesis, long time stripping experiments were performed on the WE side. Figure 8a shows the evolution of the area specific resistance during 6 h lithium stripping, corresponding to the anodic dissolution of an approx.  $3 \mu\text{m}$  thick Li layer. No external load was applied during this experiment. At the beginning, the evolution of the interface resistance is similar to the short time cycling experiments with a decreasing slope of  $dR_{\text{int}}/dt$  at the beginning. However, after 2 h the slope increases again. As  $R_{\text{int}}$  includes the load bearing contact area, its absolute value can be used to roughly estimate the relative contact loss and thus the relative number of lithium metal atoms in direct electrochemically active contact with the solid electrolyte  $N_{\xi=0}$  (i.e. the electrode active site number, in comparison to its initial value). Without the knowledge of the phase boundary structure, a quantitative treatment is not possible. However, an increase from initially  $\approx 50 \Omega\cdot\text{cm}^2$  to  $\approx 700 \Omega\cdot\text{cm}^2$  suggests a relative contact loss of 94 %. The temporal evolution of the contact loss is shown in Figure S8. This contact loss is additionally visible in a decrease of

the interface capacity  $C_{\text{int}}$  that can only be evaluated reliably for high  $R_{\text{int}}$  values using the Brug formula.

The slope  $dR_{\text{int}}/dt$  is dependent in a convoluted way on the microstructure/morphology of the lithium metal anode at the interface and is also affected by the highly changing local current density during the experiment (see Figure S8). A correlation of the dissolution characteristics due to the dislocation density, texture and thus the history of the lithium metal is expected and requires further investigations. The initially decreasing slope is an indication, that roughening of the lithium metal anode – caused by vacancy injection and supersaturation – leads to faster diffusion possibly due to the faster diffusion coefficient of adatoms in comparison to vacancies in the bulk as expected for a terrace-ledge-kink model.<sup>70</sup>

By applying a pressure of 35 MPa perpendicular to the interface after the contact loss, the interface can be reactivated, which is evident from the fact that the initial value of the interfacial resistance was reached again. Similar results were also found for the Li|LiI interface.<sup>23</sup> This experiment unambiguously proves that the contact loss must be caused solely by morphological instabilities i.e. pore formation at the lithium metal side and is not caused by passivation due to a chemical reaction. Upon cycling under a constant pressure of 35 MPa, the stripping does not lead to any contact loss, shown by the unchanged interface resistance (see Figure 8b). The pressure-induced plastic deformation and creep counter-acts the electrically driven contact loss and prevents pore formation in the lithium metal anode at the interface. The mechanical properties of the Li|LLZO contacts have a decisive impact on the kinetics of the lithium metal anode on solid electrolytes.

Applying high external mechanical loads may not be possible in practical applications, e.g. in batteries with lithium metal anode. To test whether the symmetric cells with ideally reversible electrodes (prepared under high pressure) can be cycled without the need for high external pressure, we executed a long time stripping experiment. Indeed, cycling without a major increase of the interface resistance was observed up to 5 h at  $100 \mu\text{A}\cdot\text{cm}^{-2}$  ( $0.5 \text{ mAh}\cdot\text{cm}^{-2}$ ) as shown in Figure 9. Afterwards the interface resistance also increased until a complete contact loss of the lithium metal anode was observed after  $\approx 12 \text{ h}$  ( $1.2 \text{ mAh}\cdot\text{cm}^{-2}$ ) corresponding to a dissolved lithium layer of  $\approx 5.8 \mu\text{m}$  thickness. The time dependent Nyquist plots show high quality of the obtained data and can be found in Figure S9.

1  
2  
3 Interestingly the initially firmly adhesive lithium foil could be delaminated easily after the  
4 complete contact loss. To investigate the morphology of the stripped lithium foil, the side facing  
5 the LLZO was investigated by using scanning electron microscopy. The initially flat surface  
6 that was pressed on the flat polished LLZO surface (see Figure 9a) shows deep etching  
7 structures after long time stripping (see Figure 9c). Similar morphological changes were also  
8 observed in liquid electrolytes, however, in the liquid system pitting does not lead to contact  
9 loss.<sup>71</sup> The etching structure will be affected by the microstructure of the lithium metal as well  
10 as the local transport properties of the underlying LLZO pellet (i.e. grain boundary regions) as  
11 well as the initial contact area. On most of the surface, complete contact loss was observed.  
12  
13  
14  
15  
16  
17  
18  
19

20 Overall, the lithium metal anode is morphologically unstable on solid electrolytes, thus forming  
21 large pores. Without external pressure, the lithium metal anode cannot be cycled reversibly at  
22 technically interesting areal capacities of  $5 \text{ mAh} \cdot \text{cm}^{-2}$  without further modification or weight-  
23 increasing host structures.<sup>72,73</sup>  
24  
25  
26  
27

28 The plating behavior does not seem to limit the kinetics as it decreases the interfacial resistance  
29 due to pore filling and thus will not have a negative impact on the cell performance and the  
30 interfacial contact. However, we observed that plating experiments on anodes that before were  
31 degraded anodically to high interface resistances leads to fast short-circuiting due to lithium  
32 metal penetration in the LLZO. This additionally shows that maintaining low interfacial  
33 resistances during anodic load is crucial for stable cycling. This is evident, because the local  
34 current density at the few remaining active sites will highly increase for a partially out-of-  
35 contact electrode because of increasing current constriction. It is hence difficult to compare  
36 critical current densities (CCDs) in literature due to possibly highly different load bearing  
37 contact areas. We suggest that a critical overpotential seems to be a better descriptor for lithium  
38 metal infiltration.<sup>74</sup> A very recent publication by Wang et al. already pointed out the possible  
39 role of lithium vacancy diffusion in the metal propagation behavior, controlling the CCDs  
40 observed in literature.<sup>38</sup>  
41  
42  
43  
44  
45  
46  
47  
48  
49  
50  
51  
52  
53  
54  
55  
56  
57  
58  
59  
60



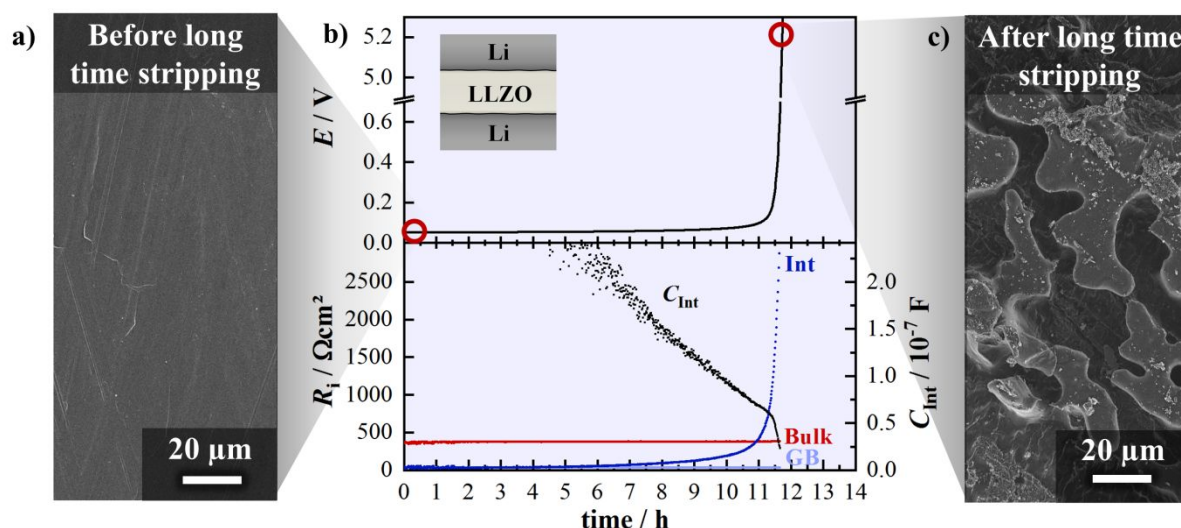
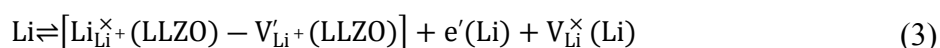


*Figure 9: Morphology of the lithium metal anode side facing the solid electrolyte before assembling the cell (a) and after long time stripping at  $100 \mu\text{A}\cdot\text{cm}^{-2}$  anodic load (WE prepared under high pressure, no pressure applied during stripping), showing morphological instability and the etching structure caused by pore formation (c). The potential profile as well as the extracted impedance contributions show a complete contact loss after around 12 h of stripping corresponding to  $1.2 \text{ mAh}\cdot\text{cm}^{-2}$  and a deposited lithium layer thickness of  $5.8 \mu\text{m}$  (b).*

**Discussion – Kinetic Model of the Interface under Anodic Load.** Different mechanisms can be envisioned for the better understanding of the dynamic behavior during metal dissolution, as schematically shown in Figure 10. The key elementary process that takes place directly at the interface under anodic polarization can be denoted using Kroeger-Vink-Notation as (Equation 3):



A lithium ion passes the Li|LLZO interface, leaving an electron  $e'(\text{Li})$  and a vacant site  $\text{V}_{\text{Li}}^{\times}(\text{Li})$  in the lithium metal (surface), while the ion is occupying an available vacant site  $\text{V}_{\text{Li}}^{\times+}(\text{LLZO})$  or an interstitial site in the topmost LLZO layer. Thus every stripped metal ion leaves one vacant site in the lithium metal anode. These vacancies can either annihilate at a site of repeatable growth (dislocations or grain boundaries) or diffuse from the interface into the metal bulk. As the charge transfer step itself appears to be not limiting and the bulk  $\text{Li}^+$  ion mobility in the SE is very high due to the superionic behavior of LLZO, vacancy diffusion<sup>75</sup> will dominate the dynamics of the interface if we exclude vacancy annihilation at this point for the sake of simplicity. If the diffusion coefficient of vacancies is high enough, the externally applied local



current density does not approach the diffusion limitation of metal dissolution (See Figure 10a), a stationary vacancy concentration at the interface is established and the interface remains morphologically stable. The polarization resistance remains constant and no contact loss will be observed.

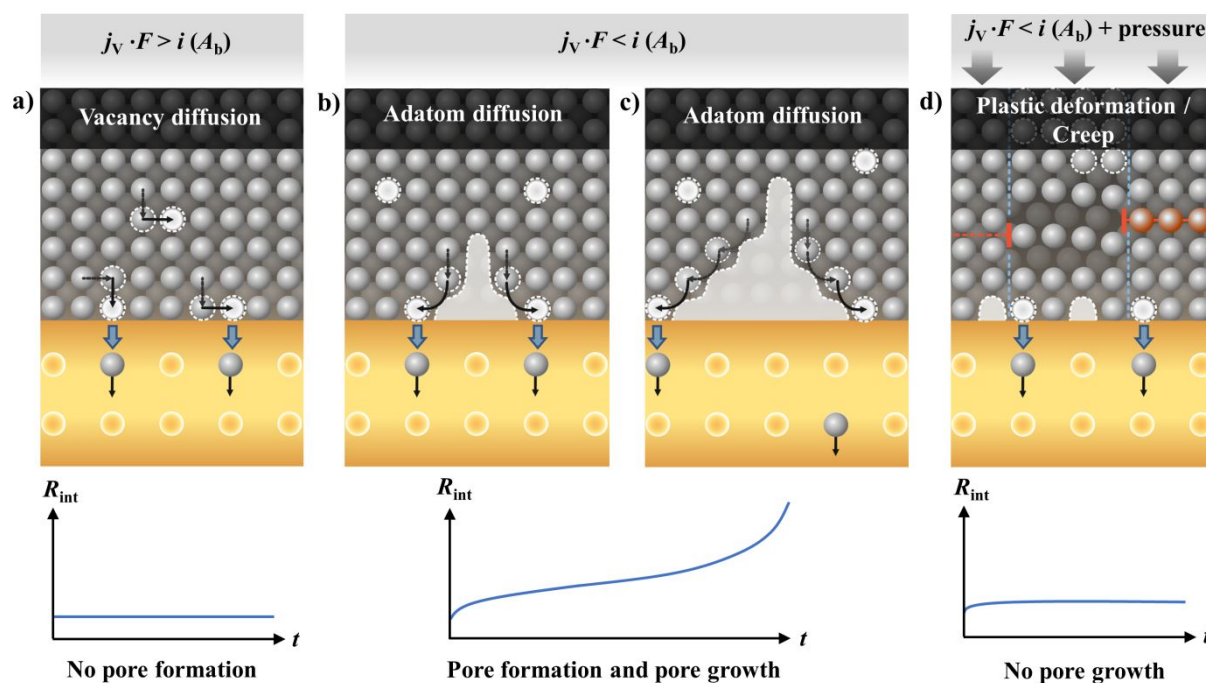


Figure 10: Schematic of the different mechanisms that facilitate charge transfer at the lithium metal anode under anodic load (limiting cases): a) If the local current density does not exceed the vacancy diffusion limit in the metal, the interface remains structurally stable. b), c) If the externally applied local current density exceeds the diffusion limit, vacancies supersaturate and accumulate to pores near the interface, that will grow and lead to increasing contact loss. Herein adatom diffusion of the metal pore surface may cause a second, higher diffusion limit. d) If external pressure is applied, pores will be annihilated due to plastic deformation of lithium metal and contact loss is restricted.

The critical anodic current density  $i_{crit}$  can be estimated as limiting flux caused by metal vacancy diffusion  $j_V$  using a defect relaxation model introduced by Schmalzried and Janek (Equation 4) where V denotes  $V_{Li}$  in the metal.<sup>76</sup>

$$j_V = \left(1 - \frac{c_V(\xi = 0)}{c_V^0}\right) c_V^0 \sqrt{\frac{D_V}{\tau_V}} \quad (4)$$

$$i_{crit} = z \cdot F \cdot j_V \quad (5)$$

Herein  $\tau_V$  is the relaxation time for the establishment of the vacancy equilibrium concentration in the metal. The equilibrium bulk concentration of vacancies is denoted as  $c_V^0$  and  $D_V$  is the diffusion coefficient of metal vacancies and can be derived from  $D_V = D_{Li} \cdot x_V^{-1}$ . The limiting flux  $j_{V,crit}$  under anodic load is defined when the concentration of the vacancies at the interphase  $c_V(\xi = 0)$  reaches a maximum value i.e. a maximum degree of vacancy supersaturation is achieved. With a vacancy diffusion coefficient of around  $10^{-10} \text{ cm}^2 \cdot \text{s}^{-1}$  at room temperature<sup>23,77–79</sup> and an equilibrium vacancy concentration of  $c_V^0 \approx 8 \cdot 10^{-9} \text{ mol} \cdot \text{cm}^{-3}$  estimated by *ab initio* calculations<sup>75</sup> we calculated the limiting current density as function the supersaturation as shown in Figure 11b. The relaxation time  $\tau_V$  of lithium vacancies was yet not experimentally measured but was assumed to be approximately 5 s, half the value of  $\tau_V$  for silver vacancies at 800 °C. This seems reasonable because the diffusion coefficient of silver at this temperature is half as high as for lithium at room temperature.<sup>80</sup>

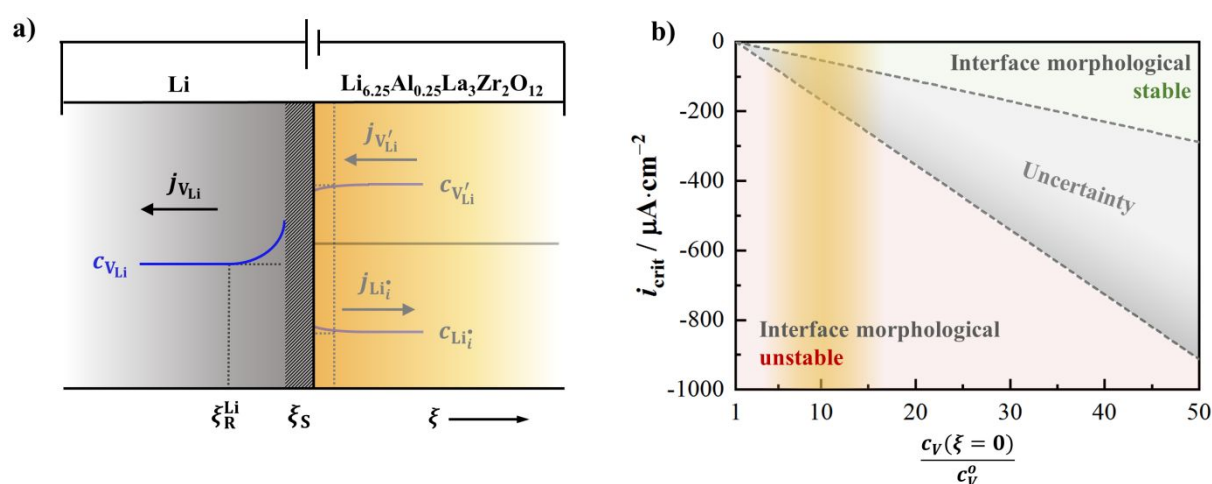


Figure 11: a) General scheme of the vacancy relaxation model after Schmalzried and Janek.<sup>76</sup>  $\xi_R^{Li}$  and  $\xi_S$  mark the defect relaxation zone in the lithium metal and a structural relaxation zone caused by non-equilibrium defects as pores, respectively. Due to vacancy supersaturation at the interface, a vacancy concentration gradient  $\nabla c_{V,Li}$  will build up at the metal anode side under anodic load, which will cause a diffusive flux  $j_{V,Li}$  of the vacancies. On the other hand also a relaxation process of the injected lithium interstitials or depleted lithium vacancies has to take place in the solid electrolyte. But due to the superionic nature of LLZO, this process will be significantly faster and no significant concentration gradient will build up. b) Calculated critical current density (grey area indicates uncertainty of parameters) vs the degree of vacancy supersaturation at the electrode. The orange highlighted area shows reasonable values for the supersaturation level that can be achieved, therefore the superposition of the orange and grey

1  
2  
3 *areas will define the limiting current density for a stable interface at room temperature. This*  
4 *estimation is, however, only applicable at room temperature and without application of*  
5 *external pressure.*  
6  
7

8  
9  
10 Figure 11 shows that at room temperature only a small current density in the range of roughly  
11  $(50 - 200) \mu\text{A}\cdot\text{cm}^{-2}$  will be possible under which the interface can remain morphologically  
12 stable when no external force is applied. If the externally applied current density exceeds this  
13 vacancy diffusion limit, the interface becomes morphologically unstable as vacancies will  
14 supersaturate and accumulate to pores near the interface. This is schematically shown in  
15 Figure 10b and c. As adatom diffusion along pore surfaces will be faster than bulk vacancy  
16 diffusion (terrace-ledge-kink model, lower activation barriers for self-diffusion along  
17 surfaces<sup>75,81</sup>) pores will grow three-dimensional and prevent a direct contact loss of the  
18 interface. Without this pore diffusion mechanism only one monolayer of lithium metal could  
19 be stripped and the effect of contact loss would lead to an extremely high polarization resistance  
20 very quickly. Due to the surface tension of the lithium metal, pores will accumulate, driven by  
21 electrochemical Ostwald ripening.<sup>25</sup> On the one hand, if the load bearing contact area will reach  
22 a limiting value, further stripping at further increasing local current densities will lead to  
23 complete contact loss. On the other hand, if an external pressure is applied, pore formation can  
24 be prevented due to plastic deformation and creep of lithium metal (see Figure 10d). Recent  
25 papers by Masias et al. and LePage et al. show that the creep behavior seems to be controlled  
26 by dislocation climbing which itself is rate-limited by vacancy diffusion.<sup>30,31</sup> In addition, the  
27 temperature will also highly affect the critical anodic current density. Due to the exponential  
28 temperature dependency of  $c_V^0$ ,  $D_V$  and  $\tau_V$ , the overall dependency is highly convoluted,  
29 however an exponential increase of  $i_{\text{crit}}$  with temperature can be expected. The pressure  
30 dependency will be also affected by temperature effects, as the elastic properties and the creep  
31 behavior is also highly temperature dependent.<sup>31</sup> Overall, the vacancy diffusion in the lithium  
32 metal anode can be considered as the key controlling transport step in the electrode kinetics in  
33 general.  
34  
35  
36  
37  
38  
39  
40  
41  
42  
43  
44  
45  
46  
47  
48  
49  
50

## 51 52 53 CONCLUSIONS 54

55  
56 The results of our experiments on pressure-controlled polarization and impedance add  
57 important insight in the chemo-mechanics of the Li|LLZO interface and highlight fundamental  
58  
59  
60

aspects of the lithium metal anode under anodic load that have severe consequences for the application in solid-state batteries with a lithium metal anode.

We demonstrate that constriction resistances at small contact spots are responsible for the high interfacial resistances of the Li|LLZO interface at low applied pressure. We suggest that the interface resistance strongly depends on the shape and size of the active contact area and the ionic conductivity of the solid electrolyte, if no contamination layers additionally hinders the charge transfer. The observation of an activation barrier for the interface impedance that is only slightly higher than the activation barrier of ion transport in the LLZO bulk, as well as the observed pressure dependence underline this hypothesis and suggest that the charge transfer step itself – i.e. the exchange of a lithium atom between the metal lattice and the SE lattice (and its oxidation or reduction) – has only a very small polarization resistance. Forming the Li|LLZO interface at high pressure, the interface resistance is found to be negligibly small, even after complete relaxation of the pressure additionally showing the strongly adhesive forces of the two phases. This result clearly highlights that the interface resistance and the corresponding activation barrier will strongly depend on the bulk transport in the constriction zone (i.e. near the interface) and thus will be severely affected by lattice distortions for example due to proton exchange, that was shown to mainly occur at the surface regions even if no contamination layers are present.<sup>82</sup>

Although these findings suggest that the fundamental Li|LLZO interface charge transfer kinetics do not interfere with high-rate capable lithium metal anodes and encourages the development of solid-state lithium metal batteries, we observe that the vacancy diffusion limitation in the lithium metal leads to an deterioration of the interface under high anodic load which – on the cell level – will highly increase the internal resistance of solid-state batteries during discharge. Morphological instabilities due to vacancy injection, accumulation and pore formation as well as the associated contact loss were found to be responsible for the increase of the interfacial impedance. Therefore, the vacancy diffusion coefficient of lithium metal is identified as the fundamental physico-chemical limitation of the lithium metal anode under anodic load. Nevertheless, pressure induced plastic deformation of the lithium metal during cycling helps to maintain the interface contact by the annihilation of pores (i.e. of vacancy aggregates). We note that plastic deformation by creep will also depend on vacancy motion – so that the role of metal vacancies may have been underrated considerably up to now.

As high stack pressures are not always technically applicable or wanted, new concepts to increase the vacancy diffusion limit in lithium metal – or to overcome it – are necessary. Strictly speaking, all these considerations apply only to the interface with pure lithium metal. The role of lithium alloying interlayers on the diffusion processes of lithium vacancies should not be overlooked and need to be further investigated.<sup>14,15,17,18,83–85</sup> Overall, this work highlights that future research should also focus on the transport and morphological instability of the lithium metal anode side

## ASSOCIATED CONTENT

### Supporting Information

Experimental setups for pressure dependent measurements, detailed structural and microstructural characterization of the LLZO pellets, scanning electron microscopy images of Li|LLZO interface cross sections, temperature dependent Nyquist plots and the corresponding Arrhenius plots, tables summarizing all impedance fit parameters, results of temperature dependent lithium stripping plating experiments for symmetric cells with ideally reversible electrodes, a graph showing the evolution of contact loss for a lithium stripping experiment, time dependent Nyquist plots during a long time lithium stripping experiment.

## AUTHOR INFORMATION

### Corresponding Authors

\*juergen.janek@phys.chemie.uni-giessen.de;

### Notes

The authors declare no competing financial interests.

## ACKNOWLEDGMENTS

The authors thank Dr. Raimund Koerver and Harald Weigand for the development of the apparatus for *operando* measurements with constant force. This work has been partly funded

by the German Federal Ministry of Education and Research (BMBF) under the project “EvaBatt”, grant identifier 03XP0134C. T. K. acknowledges the financial support (Kékulé scholarship) by the Funds of the Chemical Industry (FCI).

## REFERENCES

- (1) Xu, K. Nonaqueous Liquid Electrolytes for Lithium-Based Rechargeable Batteries. *Chem. Rev.* **2004**, *104*, 4303–4418.
- (2) Nishikawa, K.; Mori, T.; Nishida, T.; Fukunaka, Y.; Rosso, M.; Homma, T. In Situ Observation of Dendrite Growth of Electrodeposited Li Metal. *J. Electrochem. Soc.* **2010**, *157*, A1212–A1217.
- (3) Tarascon, J.-M.; Armand, M. Issues and Challenges Facing Rechargeable Lithium Batteries. *Materials For Sustainable Energy: A Collection of Peer-Reviewed Research and Review Articles from Nature Publishing Group*; World Scientific, 2011; pp 171–179.
- (4) Takeda, Y.; Yamamoto, O.; Imanishi, N. Lithium Dendrite Formation on a Lithium Metal Anode from Liquid, Polymer and Solid Electrolytes. *Electrochemistry* **2016**, *84*, 210–218.
- (5) Monroe, C.; Newman, J. The Effect of Interfacial Deformation on Electrodeposition Kinetics. *J. Electrochem. Soc.* **2004**, *151*, A880–A886.
- (6) Zhu, Y.; He, X.; Mo, Y. Origin of Outstanding Stability in the Lithium Solid Electrolyte Materials: Insights from Thermodynamic Analyses Based on First-Principles Calculations. *ACS Appl. Mater. Interfaces* **2015**, *7*, 23685–23693.
- (7) Wenzel, S.; Leichtweiss, T.; Krüger, D.; Sann, J.; Janek, J. Interphase Formation on Lithium Solid Electrolytes—an In Situ Approach to Study Interfacial Reactions by Photoelectron Spectroscopy. *Solid State Ionics* **2015**, *278*, 98–105.
- (8) Zhu, Y.; Connell, J. G.; Tepavcevic, S.; Zapol, P.; Garcia-Mendez, R.; Taylor, N. J.; Sakamoto, J.; Ingram, B. J.; Curtiss, L. A.; Freeland, J. W. Dopant-Dependent Stability of Garnet Solid Electrolyte Interfaces with Lithium Metal. *Adv. Energy Mater.* **2019**, 1803440.
- (9) Murugan, R.; Thangadurai, V.; Weppner, W. Fast Lithium Ion Conduction in Garnet-Type  $\text{Li}_7\text{La}_3\text{Zr}_2\text{O}_{12}$ . *Angew. Chem. Int. Ed.* **2007**, *46*, 7778–7781.
- (10) Cheng, L.; Crumlin, E. J.; Chen, W.; Qiao, R.; Hou, H.; Franz Lux, S.; Zorba, V.; Russo, R.; Kostecki, R.; Liu, Z.; Persson, K.; Yang, W.; Cabana, J.; Richardson, T.; Chen, G.; Doeff, M. The Origin of High Electrolyte-Electrode Interfacial Resistances in Lithium Cells Containing Garnet Type Solid Electrolytes. *Phys. Chem. Chem. Phys.* **2014**, *16*, 18294–18300.
- (11) Sharafi, A.; Yu, S.; Naguib, M.; Lee, M.; Ma, C.; Meyer, H. M.; Nanda, J.; Chi, M.; Siegel, D. J.; Sakamoto, J. Impact of Air Exposure and Surface Chemistry on  $\text{Li}-\text{Li}_7\text{La}_3\text{Zr}_2\text{O}_{12}$  Interfacial Resistance. *J. Mater. Chem. A* **2017**, *5*, 13475–13487.
- (12) Sharafi, A.; Kazyak, E.; Davis, A. L.; Yu, S.; Thompson, T.; Siegel, D. J.; Dasgupta, N. P.; Sakamoto, J. Surface Chemistry Mechanism of Ultra-Low Interfacial Resistance in the Solid-State Electrolyte  $\text{Li}_7\text{La}_3\text{Zr}_2\text{O}_{12}$ . *Chem. Mater.* **2017**, *29*, 7961–7968.
- (13) Han, X.; Gong, Y.; Fu, K. K.; He, X.; Hitz, G. T.; Dai, J.; Pearse, A.; Liu, B.; Wang, H.; Rubloff, G. Negating Interfacial Impedance in Garnet-Based Solid-State Li Metal Batteries. *Nat. Mater.* **2017**, *16*, 572–579.

- (14) Luo, W.; Gong, Y.; Zhu, Y.; Fu, K. K.; Dai, J.; Lacey, S. D.; Wang, C.; Liu, B.; Han, X.; Mo, Y. Transition from Superlithiophobicity to Superlithiophilicity of Garnet Solid-State Electrolyte. *J. Am. Chem. Soc.* **2016**, *138*, 12258–12262.
- (15) Luo, W.; Gong, Y.; Zhu, Y.; Li, Y.; Yao, Y.; Zhang, Y.; Fu, K. K.; Pastel, G.; Lin, C.-F.; Mo, Y.; Wachsman, E. D.; Hu, L. Reducing Interfacial Resistance between Garnet-Structured Solid-State Electrolyte and Li-Metal Anode by a Germanium Layer. *Adv Mater.* **2017**, *29*, 1606042.
- (16) Wang, C.; Gong, Y.; Liu, B.; Fu, K.; Yao, Y.; Hitz, E.; Li, Y.; Dai, J.; Xu, S.; Luo, W.; Wachsman, E. D.; Hu, L. Conformal, Nanoscale ZnO Surface Modification of Garnet-Based Solid-State Electrolyte for Lithium Metal Anodes. *Nano letters* **2017**, *17*, 565–571.
- (17) Fu, K. K.; Gong, Y.; Liu, B.; Zhu, Y.; Xu, S.; Yao, Y.; Luo, W.; Wang, C.; Lacey, S. D.; Dai, J. Toward Garnet Electrolyte-Based Li Metal Batteries: An Ultrathin, Highly Effective, Artificial Solid-State Electrolyte/Metallic Li Interface. *Sci. Adv.* **2017**, *3*, e1601659.
- (18) Tsai, C.-L.; Roddatis, V.; Chandran, C. V.; Ma, Q.; Uhlenbruck, S.; Bram, M.; Heitjans, P.; Guillon, O. Li<sub>7</sub>La<sub>3</sub>Zr<sub>2</sub>O<sub>12</sub> Interface Modification for Li Dendrite Prevention. *ACS Appl. Mater. Interfaces* **2016**, *8*, 10617–10626.
- (19) Wang, C.; Xie, H.; Zhang, L.; Gong, Y.; Pastel, G.; Dai, J.; Liu, B.; Wachsman, E. D.; Hu, L. Universal Soldering of Lithium and Sodium Alloys on Various Substrates for Batteries. *Adv. Energy Mater.* **2017**, *114*, 1701963.
- (20) Shen, Y.; Zhang, Y.; Han, S.; Wang, J.; Peng, Z.; Chen, L. Unlocking the Energy Capabilities of Lithium Metal Electrode with Solid-State Electrolytes. *Joule* **2018**, *2*, 1674–1689.
- (21) Yonemoto, F.; Nishimura, A.; Motoyama, M.; Tsuchimine, N.; Kobayashi, S.; Iriyama, Y. Temperature Effects on Cycling Stability of Li Plating/Stripping on Ta-Doped Li<sub>7</sub>La<sub>3</sub>Zr<sub>2</sub>O<sub>12</sub>. *J. Power Sources* **2017**, *343*, 207–215.
- (22) Koshikawa, H.; Matsuda, S.; Kamiya, K.; Miyayama, M.; Kubo, Y.; Uosaki, K.; Hashimoto, K.; Nakanishi, S. Dynamic Changes in Charge-Transfer Resistance at Li Metal/Li<sub>7</sub>La<sub>3</sub>Zr<sub>2</sub>O<sub>12</sub> Interfaces During Electrochemical Li Dissolution/Deposition Cycles. *J. Power Sources* **2018**, *376*, 147–151.
- (23) Jow, T. R.; Liang, C. C. Interface Between Solid Electrode and Solid Electrolyte - A Study of the Li/LiI (Al<sub>2</sub>O<sub>3</sub>) Solid-Electrolyte System. *J. Electrochem. Soc.* **1983**, *130*, 737–740.
- (24) Janek, J. Zum Ladungsdurchtritt an Phasengrenzen in Festkörpern. Habilitation, Universität Hannover, Hannover, 1997.
- (25) Schröder, A.; Fleig, J.; Gryaznov, D.; Maier, J.; Sitte, W. Quantitative Model of Electrochemical Ostwald Ripening and its Application to the Time-Dependent Electrode Potential of Nanocrystalline Metals. *J. Phys. Chem. B* **2006**, *110*, 12274–12280.
- (26) Eichinger, G. Electrochemical Investigation on the Contact in Solid State Cells with an RbAg<sub>4</sub>I<sub>5</sub> Electrolyte. *J. Appl. Electrochem.* **1980**, *10*, 239–244.
- (27) Janek, J.; Majoni, S. Investigation of Charge Transport Across the Ag|AgI-interface:(I) Occurrence of Periodic Phenomena During Anodic Dissolution of Silver. *Berichte der Bunsengesellschaft für physikalische Chemie* **1995**, *99*, 14–20.

- (28) *Influence of Mechanical Pressure on Ionic Charge Transport Across the Ag| AgI-Interface-Periodic Oscillations of Interfacial Properties*; Janek, J.; Majoni, S., Eds.; Trans Tech Publ, 1996.
- (29) Janek, J. Oscillatory Kinetics at Solid/Solid Phase Boundaries in Ionic Crystals. *Solid State Ionics* **2000**, *131*, 129–142.
- (30) Masias, A.; Felten, N.; Garcia-Mendez, R.; Wolfenstine, J.; Sakamoto, J. Elastic, Plastic, and Creep Mechanical Properties of Lithium Metal. *J Mater Sci* **2018**, *166*, A89-A97.
- (31) LePage, W. S.; Chen, Y.; Kazyak, E.; Chen, K.-H.; Sanchez, A. J.; Poli, A.; Arruda, E. M.; Thouless, M. D.; Dasgupta, N. P. Lithium Mechanics: Roles of Strain Rate and Temperature and Implications for Lithium Metal Batteries. *J. Electrochem. Soc.* **2019**, *166*, A89-A97.
- (32) Wenzel, S.; Randau, S.; Leichtweiß, T.; Weber, D. A.; Sann, J.; Zeier, W. G.; Janek, J. Direct Observation of the Interfacial Instability of the Fast Ionic Conductor  $\text{Li}_{10}\text{GeP}_2\text{S}_{12}$  at the Lithium Metal Anode. *Chem. Mater.* **2016**, *28*, 2400–2407.
- (33) Wenzel, S.; Sedlmaier, S. J.; Dietrich, C.; Zeier, W. G.; Janek, J. Interfacial Reactivity and Interphase Growth of Argyrodite Solid Electrolytes at Lithium Metal Electrodes. *Solid State Ionics* **2018**, 102–112.
- (34) Wenzel, S.; Weber, D. A.; Leichtweiss, T.; Busche, M. R.; Sann, J.; Janek, J. Interphase Formation and Degradation of Charge Transfer Kinetics between a Lithium Metal Anode and Highly Crystalline  $\text{Li}_7\text{P}_3\text{S}_{11}$  Solid Electrolyte. *Solid State Ionics* **2016**, *286*, 24–33.
- (35) Sharafi, A.; Meyer, H. M.; Nanda, J.; Wolfenstine, J.; Sakamoto, J. Characterizing the  $\text{Li}$ - $\text{Li}_7\text{La}_3\text{Zr}_2\text{O}_{12}$  Interface Stability and Kinetics as a Function of Temperature and Current Density. *J. Power Sources* **2016**, *302*, 135–139.
- (36) Buschmann, H.; Berendts, S.; Mogwitz, B.; Janek, J. Lithium Metal Electrode Kinetics and Ionic Conductivity of the Solid Lithium Ion Conductors “ $\text{Li}_7\text{La}_3\text{Zr}_2\text{O}_{12}$ ” and  $\text{Li}_{7-x}\text{La}_3\text{Zr}_{2-x}\text{Ta}_x\text{O}_{12}$  with Garnet-Type Structure. *J. Power Sources* **2012**, *206*, 236–244.
- (37) Slade, P. G. *Electrical Contacts: Principles and Applications*; CRC press, 2017.
- (38) Wang, M.; Wolfenstine, J. B.; Sakamoto, J. Temperature Dependent Flux Balance of the  $\text{Li}/\text{Li}_7\text{La}_3\text{Zr}_2\text{O}_{12}$  Interface. *Electrochim. Acta* **2019**, *296*, 842–847.
- (39) Galven, C.; Dittmer, J.; Suard, E.; Le Berre, F.; Crosnier-Lopez, M.-P. Instability of Lithium Garnets against Moisture. Structural Characterization and Dynamics of  $\text{Li}_{7-x}\text{H}_x\text{La}_3\text{Sn}_2\text{O}_{12}$  and  $\text{Li}_{5-x}\text{H}_x\text{La}_3\text{Nb}_2\text{O}_{12}$ . *Chem. Mater.* **2012**, *24*, 3335–3345.
- (40) Jin, Y.; McGinn, P. J.  $\text{Li}_7\text{La}_3\text{Zr}_2\text{O}_{12}$  Electrolyte Stability in Air and Fabrication of a  $\text{Li}/\text{Li}_7\text{La}_3\text{Zr}_2\text{O}_{12}/\text{Cu}_{0.1}\text{V}_2\text{O}_5$  Solid-State Battery. *J. Power Sources* **2013**, *239*, 326–331.
- (41) Pawley, G. S. Unit-Cell Refinement from Powder Diffraction Scans. *J. Appl. Cryst.* **1981**, *14*, 357–361.
- (42) Coelho, A. A. Topas-Academic. *Coelho Software, Brisbane, Australia* **2007**.
- (43) Simon, F. J.; Blume, L.; Hanauer, M.; Sauter, U.; Janek, J. Development of a Wire Reference Electrode for Lithium All-Solid-State Batteries with Polymer Electrolyte: FEM Simulation and Experiment. *J. Electrochem. Soc.* **2018**, *165*, A1363-A1371.
- (44) Winkler, J.; Hendriksen, P. V.; Bonanos, N.; Mogensen, M. Geometric Requirements of Solid Electrolyte Cells with a Reference Electrode. *J. Electrochem. Soc.* **1998**, *145*, 1184–1192.



- (45) Adler, S. B. Reference Electrode Placement in Thin Solid Electrolytes. *J. Electrochem. Soc.* **2002**, *149*, E166-E172.
- (46) Rutman, J.; Riess, I. Placement of Reference Electrode in Solid State Electrolyte Cells. *Solid State Ionics* **2008**, *179*, 913–918.
- (47) Ishiguro, K.; Nemori, H.; Sunahiro, S.; Nakata, Y.; Sudo, R.; Matsui, M.; Takeda, Y.; Yamamoto, O.; Imanishi, N. Ta-Doped  $\text{Li}_7\text{La}_3\text{Zr}_2\text{O}_{12}$  for Water-Stable Lithium Electrode of Lithium-Air Batteries. *J. Electrochem. Soc.* **2014**, *161*, A668-A674.
- (48) Sudo, R.; Nakata, Y.; Ishiguro, K.; Matsui, M.; Hirano, A.; Takeda, Y.; Yamamoto, O.; Imanishi, N. Interface Behavior Between Garnet-Type Lithium-Conducting Solid Electrolyte and Lithium Metal. *Solid State Ionics* **2014**, *262*, 151–154.
- (49) Ishiguro, K.; Nakata, Y.; Matsui, M.; Uechi, I.; Takeda, Y.; Yamamoto, O.; Imanishi, N. Stability of Nb-Doped Cubic  $\text{Li}_7\text{La}_3\text{Zr}_2\text{O}_{12}$  with Lithium Metal. *J. Electrochem. Soc.* **2013**, *160*, A1690-A1693.
- (50) Meyer, M.; Rickert, H.; Schwaitzer, U. Investigations on the Kinetics of the Anodic Dissolution of Lithium at the Interface  $\text{Li}/\text{Li}_3\text{N}$ . *Solid State Ionics* **1983**, *9*, 689–693.
- (51) AZoM. Lithium (Li)-Properties, Applications. <https://www.azom.com/article.aspx?ArticleID=9101> (accessed October 23, 2018).
- (52) Samsonov, G. V. Mechanical Properties of the Elements. *Handbook of the Physicochemical Properties of the Elements*; Springer, 1968; pp 387–446.
- (53) Wang, M.; Sakamoto, J. Correlating the Interface Resistance and Surface Adhesion of the Li Metal-Solid Electrolyte Interface. *J. Power Sources* **2018**, *377*, 7–11.
- (54) Xu, C.; Ahmad, Z.; Aryanfar, A.; Viswanathan, V.; Greer, J. R. Enhanced Strength and Temperature Dependence of Mechanical Properties of Li at Small Scales and its Implications for Li Metal Anodes. *PNAS* **2017**, *114*, 57–61.
- (55) Schultz, R. P. *Lithium: Measurement of Young's Modulus and Yield Strength*, 2002.
- (56) *Li Material Testing-Fermilab Antiproton Source Lithium Collection Lens*; Tariq, S.; Ammigan, K.; Hurh, P.; Schultz, R.; Liu, P.; Shang, J., Eds.; IEEE, 2003.
- (57) Boyer, L.; Noel, S.; Houze, F. Constriction Resistance of a Multispot Contact: an Improved Analytical Expression. *IEEE Transactions on Components, Hybrids, and Manufacturing Technology* **1991**, *14*, 134–136.
- (58) Narayan, S.; Anand, L. A Large Deformation Elastic–Viscoplastic Model for Lithium. *Extreme Mechanics Letters* **2018**, *24*, 21–29.
- (59) Fleig, J.; Maier, J. The Influence of Laterally Inhomogeneous Contacts on the Impedance of Solid Materials: A Three-Dimensional Finite-Element Study. *J. Electroceram.* **1997**, *1*, 73–89.
- (60) Irvine, J. T. S.; Sinclair, D. C.; West, A. R. Electroceramics: Characterization by Impedance Spectroscopy. *Advanced Materials* **1990**, *2*, 132–138.
- (61) Fleig, J.; Pham, P.; Sztulzaft, P.; Maier, J. Inhomogeneous Current Distributions at Grain Boundaries and Electrodes and their Impact on the Impedance. *Solid State Ionics* **1998**, *113*, 739–747.
- (62) Fleig, J. Impedance Spectroscopy on Solids: The Limits of Serial Equivalent Circuit Models. *J. Electroceramics* **2004**, *13*, 637–644.
- (63) Fleig, J.; Maier, J. Point Contacts in Solid State Ionics: Finite Element Calculations and Local Conductivity Measurements. *Solid State Ionics* **1996**, *86*, 1351–1356.

- (64) Brug, G. J.; van Den Eeden, A. L.; Sluyters-Rehbach, M.; Sluyters, J. H. The Analysis of Electrode Impedances Complicated by the Presence of a Constant Phase Element. *J. Electroanal. Chem.* **1984**, *176*, 275–295.
- (65) Yu, S.; Siegel, D. J. Grain Boundary Contributions to Li-Ion Transport in the Solid Electrolyte  $\text{Li}_7\text{La}_3\text{Zr}_2\text{O}_{12}$  (LLZO). *Chem. Mater.* **2017**, *29*, 9639–9647.
- (66) Raleigh, D. O. Electrode Processes in Solid Electrolyte Systems. *Electroanal. Chem.* **1971**, *6*, 87–186.
- (67) Lushta, V.; Dietzel, D.; Roling, B.; Schirmeisen, A. Nanoscale Characterization of Ion Mobility by Temperature Controlled Li-Nanoparticle Growth. *ACS Appl. Mater. Interfaces* **2019**, *11*, 5476–5483.
- (68) Ma, C.; Cheng, Y.; Yin, K.; Luo, J.; Sharafi, A.; Sakamoto, J.; Li, J.; More, K. L.; Dudney, N. J.; Chi, M. Interfacial Stability of Li Metal–Solid Electrolyte Elucidated via in Situ Electron Microscopy. *Nano Lett* **2016**, *16*, 7030–7036.
- (69) Klerk, N. J. J. de; Wagemaker, M. Space-Charge Layers in All-Solid-State Batteries; Important or Negligible? *ACS Appl. energy Mater.* **2018**, *1*, 5609–5618.
- (70) Knacke, O.; Stranski, I. N. Die Theorie des Kristallwachstums. *Erg. Exakt. Naturwiss.* **1952**, *26*, 383–427.
- (71) Gireaud, L.; Grugeon, S.; Laruelle, S.; Yrieix, B.; Tarascon, J.-M. Lithium Metal Stripping/Plating Mechanisms Studies: A Metallurgical Approach. *Electrochem. Commun.* **2006**, *8*, 1639–1649.
- (72) Albertus, P.; Babinec, S.; Litzelman, S.; Newman, A. Status and Challenges in Enabling the Lithium Metal Electrode for High-Energy and Low-Cost Rechargeable Batteries. *Nat. Energy* **2018**, *3*, 16–21.
- (73) Hitz, G. T.; McOwen, D. W.; Zhang, L.; Ma, Z.; Fu, Z.; Wen, Y.; Gong, Y.; Dai, J.; Hamann, T. R.; Hu, L. High-Rate Lithium Cycling in a Scalable Trilayer Li-Garnet-Electrolyte Architecture. *Mater. Today* **2018**, *22*, 50–57.
- (74) Han, F.; Westover, A. S.; Yue, J.; Fan, X.; Wang, F.; Chi, M.; Leonard, D. N.; Dudney, N. J.; Wang, H.; Wang, C. High Electronic Conductivity as the Origin of Lithium Dendrite Formation within Solid Electrolytes. *Nat. Energy* **2019**.
- (75) Frank, W.; Breier, U.; Elsässer, C.; Fähnle, M. First-Principles Calculations of Absolute Concentrations and Self-Diffusion Constants of Vacancies in Lithium. *Phys. Rev. Lett.* **1996**, *77*, 518.
- (76) Schmalzried, H.; Janek, J. Chemical Kinetics of Phase Boundaries in Solids. *Berichte der Bunsengesellschaft für physikalische Chemie* **1998**, *102*, 127–143.
- (77) Lodding, A.; Mundy, J. N.; Ott, A. Isotope Inter-Diffusion and Self-Diffusion in Solid Lithium Metal. *Phy. Status Solidi B* **1970**, *38*, 559–569.
- (78) Dologlou, E. Self-Diffusion in Solid Lithium. *Glass Phys. Chem.* **2010**, *36*, 570–574.
- (79) Messer, R.; Noack, F. Nuclear Magnetic Relaxation by Self-Diffusion in Solid Lithium:  $T_1$ -Frequency Dependence. *Appl. Phys.* **1975**, *6*, 79–88.
- (80) Fischbach, H. Leerstelleninjektion in Silber während elektrolytischen Abtrags bei hohen Temperaturen. *Z. Metallkd.* **1980**, *71*, 115–119.
- (81) Jäckle, M.; Helmbrecht, K.; Smits, M.; Stottmeister, D.; Groß, A. Self-Diffusion Barriers: Possible Descriptors for Dendrite Growth in Batteries? *Energy Environ. Sci.* **2018**, *11*, 3400–3407.

(82) Brugge, R. H.; Hekselman, A. O.; Cavallaro, A.; Pesci, F. M.; Chater, R. J.; Kilner, J. A.; Agüero, A. Garnet Electrolytes for Solid State Batteries: Visualisation of Moisture-Induced Chemical Degradation and Revealing its Impact on the Li-Ion Dynamics. *Chem. Mater.* **2018**, *20*, 3704–3713.

(83) Fu, K.; Gong, Y.; Fu, Z.; Xie, H.; Yao, Y.; Liu, B.; Carter, M.; Wachsman, E.; Hu, L. Transient Behavior of the Metal Interface in Li Metal-Garnet Batteries. *Angew. Chem. Int. Ed.* **2017**, *56*, 14942–14947.

(84) He, M.; Cui, Z.; Chen, C.; Li, Y.; Guo, X. Formation of Self-Limited, Stable and Conductive Interfaces between Garnet Electrolytes and Lithium Anodes for Reversible Lithium Cycling in Solid-State Batteries. *J. Mater. Chem. A* **2018**, *6*, 11463–11470.

(85) Koshikawa, H.; Matsuda, S.; Kamiya, K.; Miyayama, M.; Kubo, Y.; Uosaki, K.; Hashimoto, K.; Nakanishi, S. Electrochemical Impedance Analysis of the Li/Au-Li<sub>7</sub>La<sub>3</sub>Zr<sub>2</sub>O<sub>12</sub> Interface during Li Dissolution/Deposition Cycles: Effect of Pre-Coating Li<sub>7</sub>La<sub>3</sub>Zr<sub>2</sub>O<sub>12</sub> with Au. *J. Electroanal. Chem.* **2019**, *835*, 143–149.

For Table of Contents only

